NTNU
Norwegian University of
Science and Technology

Incorporation of Iron(III) in Silica Aerogels

Simeon Kristoffersen

Chemistry
Submission date: May 2016
Supervisor: Karina Mathisen, IKJ
Co-supervisor: Tina Kristiansen, IKJ

Norwegian University of Science and Technology
Department of Chemistry

Acknowledgements

First, I must thank NTNU for allowing me to write this thesis and even paying the expenses, especially IKJ and IMT for allowing me access to expensive equipment and laboratories against better judgement. I know you do this for all master students with the right grades, but looking back at how clueless I was two years ago I'm honestly surprised you did. Special thanks to Elin Albertsen, Kristin Høydalsvik and Syverin Lierhagen for tutoring me on proper use of the various instruments used for characterization.

Secondly, huge thanks to the ESRF and SNBL for allowing me to visit their synchrotron facility to run my samples. Some of the most important result of this thesis were collected there and it was undoubtedly one of the most enjoyable experiences during my 2-years as a master student. Beam time is a magical phenomenon, and Miley Cyrus' "Wrecking Ball" now holds a special place in my heart, for better or worse. Thanks to Wouter van Beek from ESRF who assisted us during beam time, as well as Kate and Said from Glasgow for being lovely supporting people.

Then, of course, huge thanks to my supervisor Karina Mathisen and my co-supervisor Tina Kristiansen. Writing a master thesis is very different from anything I have ever done before, and in the beginning, I admit, I was very bad at it. This thesis would not have happened if not for Karina and Tina giving me encouragement, and kicking my butt back into gear when I needed it. Thank you for sticking with me despite how frustrating I must have been at times.

The rest of the structural chemistry group also deserves a mention. Most of them have helped in one way or another, but just their presence and moral support has made this entire experience far more enjoyable than it otherwise would have been. So, to all the members and ex-members; Stian, Karsten, Daniel, Kenneth, Filip, Guro, Øyvind, Sondre and Joakim: Thank you for your support.

Lastly, but obligatory, a thank you to my family. Even though few of you understand what I am even doing your support was always felt. Even though I visit now and again I always miss you. I don't really say it too often but I love you all.

- Simeon Kristoffersen

Summary

English

Silica aerogels containing both single site Fe^{3+} as well as small Fe_xO_y nanoparticles of oxide/hydroxide species were synthesized from a waterglass precursor using co-precursor and ambient pressure drying techniques. Fe^{3+} was incorporated by adding ferrous nitrate to the synthesis before the sol-gel step. ICP-MS was used to measure the iron loadings of the gels, XRD was used to determine the existence of crystalline species and nitrogen adsorption was used to determine information of the surface. To determine the exact nature of the iron species the samples were analysed by UV-vis and X-ray absorption spectroscopy.

The aerogel consisted of amorphous silica with large populations of micropore and mesopores as well as some macropores and a porosity ranging from 50 to 70% for most successful samples. The iron loading for some samples were as high as 10 wt%, and addition of iron caused the average pore diameter to rise, but lowered the overall porosity. Some aerogel samples contained a crystalline species visible by XRD, and this species grew more prominent in samples with higher iron loadings.

The iron species was determined to be a mixture of largely tetrahedral single-site Fe^{3+} and nanoparticles of a oxide/hydroxide species suspected to be similar to ferrihydrite and/or hematite. Annealing caused the nanoparticles to shrink to a smaller size, hypothesized to be due to interaction with the silica surface. The exact nature of the annealed samples were left inconclusive due to noisy EXAFS data.

Norsk

Silisium oksid aerogeler med både single site Fe^{3+} og små Fe_xO_y nanopartikler av en oksid/hydroksid specie ble syntesert fra vannglass ved bruk av co-precursor og APD teknikker. Fe^{3+} ble inkorporert ved å tilsette jern(III) nitrat før sol-gel steget i syntesen. ICP-MS ble brukt til å måle jern innholdet i prøvene, XRD til å måle grad av krystallinitet og nitrogen isotermer ble målt for å analyser overflatedata. For å bekrefte hvilken type jern specie som var inkorporert ble det brukt UV-vis og røntgen absorbsjonsspektroskopi.

Aerogelene besto av amorf silisium oksid med store mengder microporer og mesoporer, en mindre mengde makroporer og porøsiteter fra 50 til 70% for de fleste av de bra prøvene. Jern innholdet varierte og var så høyt som 10 w%, og tilsetning av jern førte til en økning av den

gjennomsnittlige pore størrelse, men en mindre grad av porøsitet. Noen prøver inneholdt krystallinske specier synlige med XRD og denne specien ble tydeligere ved større jerninnhold.

Jern specien ble konkludert til å vare en blanding av inkorporerte tetraedriske Fe^{3+} single-sites og nanopartikler av en oksid/hydroksid specie som er mistenkt til å ligne ferrihydritt og/eller hematitt. Varmebehandling førte til at nanopartiklene ble enda mindre, muligens på grunn av interaksjoner med silisium oksid overflaten. Data for de varmebehandlede prøvene var dessverre for støyete til å dra endelig konklusjoner.

Common Abbreviations and Symbols

SSC	Single-site catalyst
APD	Ambient pressure drying
SCD	Super-critical drying
SA	Silisic acid
HMDSO	Hexamethyldisiloxane
HMDZ	Hexamethyldisilazane
XRD	X-ray diffraction
ICP-MS	Inductively coupled plasma mass spectrometry
BET	Brunauer-Emmet-Teller theory
BJH	Barret-Joyner-Halenda theory
UV-vis	Ultra-violet visible light absorption spectroscopy
XAS	X-ray absorption spectroscopy
XANES	X-ray absorption near edge spectroscopy
EXAFS	Extended X-ray spectroscopy fine structure
SSA (A_{BET})	Spesific surface area
V_p	Pore volume
D_p	Pore diameter
R-value	Fit index for EXAFS
N	Multiplicity
R	Shell distance
$2\sigma^2$	Debye-Waller factor
AFAC	Amplitude reduction facto for EXCURV98

Index

Acknowledgements - 3 -

Summary - 5 -

Common Abbreviations and Symbols - 7 -

Index - 9 -

1 Motivation and Aim of the Thesis - 11 -

2 Theory - 13 -

- 2.1 Silica aerogels - 13 -
- 2.2 Silica aerogel as a catalytic carrier - 14 -
- 2.3 Synthesis of silica aerogels - 16 -
  - 2.3.1 The sol-gel synthesis - 16 -
  - 2.3.2 Surface modification and drying - 18 -
- 2.4 Iron incorporation - 21 -
- 2.5 Colour of iron compounds - 24 -
- 2.6 Characterization - 25 -
  - 2.6.1 X-ray diffraction - 25 -
  - 2.6.2 Nitrogen adsorption/desorption isotherm - 26 -
  - 2.6.3 Inductively coupled plasma mass spectrometry - 28 -
  - 2.6.4 UV-vis absorption spectroscopy - 29 -
  - 2.6.5 X-ray absorption spectroscopy - 31 -

3 Experimental - 39 -

- 3.1 Synthesis - 39 -
- 3.2 Samples - 40 -
- 3.3 Characterization - 40 -
  - 3.3.1 XRD - 41 -
  - 3.3.2 Nitrogen isotherms - 41 -
  - 3.3.3 ICP-MS - 41 -
  - 3.3.4 UV-vis - 41 -
  - 3.3.5 XAS - 41 -

4 Results - 43 -

- 4.1 Simple Observations - 43 -
- 4.2 XRD Results - 45 -

4.3 Nitrogen Isotherm Results ....- 47 -
4.4 ICP-MS Results ....- 51 -
4.5 XAS Results ....- 52 -
4.6 UV-vis Results ....- 58 -
5.1 The Effect of synthesis parameters ....- 61 -
  5.1.1 Iron content ....- 61 -
  5.1.2 Other parameters ....- 63 -
5.2 The Effect of Annealing ....- 64 -
5.3 Determining the iron species ....- 65 -
  5.3.1 Considering nano-phase ....- 69 -
  5.3.2 Considering single sites ....- 71 -
  5.3.3 Considering a nano-phase and single sites combination ....- 72 -
6 Conclusion ....- 75 -
7 Future Work ....- 77 -
8 Sources ....- 79 -

1 Motivation and Aim of the Thesis

Aerogels are a group of highly versatile futuristic materials marked by very high porosities and interesting pore systems [1] while still retaining remarkable strength despite being made mostly of air [2]. The material can be made from plastics, cellulose and metal oxides, but silica aerogels, the first type ever synthesized, are especially versatile. Usually synthesized from the sol-gel method, silica aerogels are a synthetic toolbox for providing new and interesting aerogel materials [1].

In this thesis we want to explore silica aerogels' potential as a carrier material for heterogeneous processes. The material should be ideal for these purposes due to its surface properties, extensive pore system and large surface area [3]. Recent developments have made the material even more attractive, as cheaper precursors and simpler synthesis routes makes silica aerogel faster and cheaper to synthesize [4]. These methods include sodium silicate, or waterglass, as the main precursor and hydrophobic surface modification to avoid the need for super critical fluids.

Recent reports show that these cheap aerogels can take up a loading of copper by simply adding a salt to the synthesis [5], and though the resulting gels are not as porous as their expensive counterparts they serve well as catalysts [6]. Furthermore, this synthesis route produced lone copper atoms incorporated in the silica framework, so called single-sites [5, 7]. Single-site catalysts (SSC) provide unique properties that bulk materials do not possess [8, 9] and ,needless to say, for heterogeneous catalysis they cannot be made without a carrier. If silica aerogels provide a cheap route for producing catalytically capable SSC, then it is surely worth exploring.

The main aim of this thesis is to attempt the synthesis of single-site iron (III) incorporated into silica aerogel. Iron(III) was chosen due to a recent interest in the catalytic activity of single-site iron [10, 11]. Another motivator behind the choice of iron is discovering if this synthesis route is capable of producing a wider range of SSC chemically different from copper. If the method works for “noble copper” and “rusty iron” it may also work for a wide variety of transition metals, and that would be very exciting.

2 Theory

2.1 Silica aerogels

Aerogels are a group of materials made by removing the liquid from a gel matrix [12]. If done correctly this preserves the interconnected structure of the gel and leaves behind a hollow pore structure [13]. A gel is a non-fluid network, usually made from colloids or polymers, supported from within by some fluid. Aerogels are the same, except the usually liquid fluid is now gone and replaced with air. Not all gel structures can survive this process, and will collapse in a process called shrinkage [14], but those that do survive presents us with a range of interesting and useful properties [3]. The name aerogel is descriptive and fitting as most aerogel are mostly air by volume, and the material is sometimes dubbed liquid smoke due to its otherworldly appearance seen in Figure 2-1.

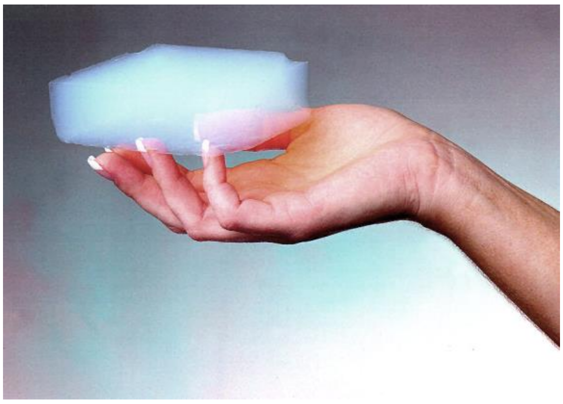

Figure 2-1: A large piece of high quality silica aerogel, also called liquid smoke due to its ghostly appearance. Courtesy NASA/JPL-Caltech.

The silica aerogel is perhaps the most common aerogel, and the first aerogel synthesized by Kistler in 1931 [12]. The material is formed from silica gel, an amorphous form of silica made from interconnected nano-sized colloids hosting an extensive water-filled pore structure. Silica gel may also be called silica hydrogel to further differentiate it from the aerogel variant, or alcogel if containing alcohol.

Silica aerogel is a material whose intricate pore structure and chemical composition combine to form a series of interesting properties [3]. Silica is a slightly acidic, electrically isolating and mostly inert material. Its chemical resistance makes it ideal for laboratory equipment, though some acids and strong bases can dissolve it. In catalysis it is used for processes at relatively low temperatures up to 300°C for reactions like polymerization, hydrogenation and oxidations [15]. Silica has a relatively lower thermal stability compared to other carrier materials e.g.

alumina and can in some cases react with water steam to form volatile hydroxides [15]. The aerogel retains these properties, but its enormous specific surface area leaves it quite vulnerable to attacks from strong bases or hydrofluoric acid. The surface area arises from the unique pore system. Silica aerogel contains a continuous pore system of both larger and smaller pores that may represent as much as 99% or more of the materials volume depending on the quality [3, 14]. This gives the material remarkable thermal insulation properties, and it is already used as home insulation as well as in space technology for this reason. The material also has remarkable mechanical properties, being strong and in some cases flexible depending on the synthesis [2, 3]. The pore volume also has a remarkable fine structure that makes the material quite interesting in terms of catalysis [3], which is our focus.

2.2 Silica aerogel as a catalytic carrier

The pore structure of silica aerogels are interconnected and hierarchical. That the material is hierarchical refers to the two separate pore size domains in the same structure; The material has two types of pores, large and small. IUPAC defines pores in three domains: Micropores are smaller than 2 nm in diameter, macropores are larger than 50 nm and mesopores are inbetween. The pore structure contains some pores in from all three domains, but it is dominated by mesopores [14] taking up most of the volume and leading into smaller micropores throughout the structure. This pore structure arises from the synthesis of the gel, and all pores connect to one another making the pore system interconnected [14].

The micropores are sometimes very useful in terms of selectivity, as they are in the size range of most molecules. Zeolites are the prime example of this, as they are catalysts containing only micropores [15]. The selectivity of zeolites arise from their consistent size ranges, and this is not a property of silica aerogels. Silica aerogels are chaotic, and the resulting micropores will be to variable to expect any consistent selectivity.

Although zeolites are supreme in terms of selectivity they are purely microporous materials, and this is their biggest drawback. A material with only micropores has a low diffusivity, and a high chance of being clogged. Mesopores or macropores are far better at dealing with these problems.

Catalysis is a surface phenomenon and catalysts are designed to expose as much of their active phase as possible [15]. This can be done by simply making the active phase porous, but this is not possible for all materials. Some catalyst have active phases in the form of isolated sites or small particles that may lose their activity in bulk form, even if made porous. In these cases the active phase is instead finely distributed on the surface of a porous carrier for the same effect creating a supported catalyst. Consider then a porous particle with catalytically active sites throughout its surface. To use this particle efficiently we must deliver reactants to the entire surface and remove the products as they form. This becomes a problem of traffic, which is where diffusivity becomes important.

If the particle contains only small micropores the diffusivity will be low, and if the activity of the catalyst is high all reactants diffusing through the particle will most likely react with an outer reaction site before reaching the centre. This causes the centre of the particle to be inactive because no reactant ever get there in time, and this is wasteful. Smaller pores can also be clogged, especially micropores. Large organic by-products can form and cause congestion, closing off and effectively deactivating areas of the catalyst. These by-products are called coke and larger pores significantly decreases deactivation by coke formation. We call this scenario a diffusion limited reaction, because it is the diffusivity, and not the catalytic activity, that limits it. This problem is considerably lessened by increasing the pore diameter into the mesopore domain, though the selective properties of the micropores may be lost. The reason for hierarchical systems being so interesting is that they may have the increased diffusivity of mesopores and selectivity of micropores.

Silica aerogels are interesting because they contain pores over all size domains. The mesopores and fewer macropores act as freeways to deliver reactants throughout the gel and removing the products, the micropores add additional surface area, though their non-uniform size range decreases the likelihood of selectivity.

Silica aerogel is slightly acidic, but is not considered very active for most reactions, acid catalysed or otherwise. Thus, the hierarchical pore structure can only be utilized properly if we introduce a catalytically active site to the silica matrix e.g. iron or some other metal.

There are many types of catalysts, but we will focus on one specific type: single site catalysts (SSC). SSC are single atoms incorporated into the lattice of a carrier. Sometimes this is called isomorphic substitution, where the new atom simply takes the place of another atom in the structure, retaining the same environment. The new atom might also create a new environment deviating from the surrounding crystal structure or sites. Single site catalysts, by definition, cannot exist without a carrier and can behave quite differently from particle or bulk catalysts [8].

2.3 Synthesis of silica aerogels

There are several ways of making silica aerogel [16], the main differences being the choice of precursors and the drying step. The standard method [3] uses expensive and toxic silicon alkoxides to form an alcogel. The alcogel is then dried by exchanging the pore fluid with supercritical CO_2 [3, 12, 14]. This method, along with other variants [14], produce high quality aerogels with high porosity and optical transmittance. Especially supercritical drying (SCD) is preferred when making larger pieces of aerogel like in figure 2-1. The SCD process is, however, quite expensive and cumbersome, not allowing for more than bulk production. If silica aerogels are to be affordably mass produced, we must find cheaper alternatives for both silicon alkoxide precursors and the SCD process [3].

The alternate synthesis route we will use, and the one developed by Kristiansen [5], is using sodium silicate, or waterglass, as our precursor. Waterglass gels have somewhat larger pores, are quite stiff and does not always produce as high quality gels as the alkoxide precursors [14]. Waterglass derived gels have long been used as a cheap alternative to the alkoxides, even by Kistler himself [3, 12, 14], and is usually combined with ambient pressure drying (APD) to further lower the costs [4, 14]. Our synthesis route uses waterglass as a precursor and APD [5].

2.3.1 The sol-gel synthesis

The synthesis of our silica aerogel begins with a silica hydrogel formed by sol-gel synthesis. A sol is a dispersion of colloids, in this case silica colloids in water. The sol can be created from several precursor solutions and we will use waterglass. The waterglass cannot be used as a direct precursor and must be ion exchanged to form silicic acid (SA) [3]. The raction for the ion exchange is shown below:

$$Na_2SiO_3 + 2H^+ \rightarrow\ H_2SiO_3 +\ 2Na^+$$

Although sodium silicate can appear as chains of three or more silicon atoms, the most comon species of silisic acid formed is, ortho-silisic acid H_2SiO_3. It will react with water to form our precursor solution, $Si(OH)_4$ (Figure 2-2). This precursor is quite similar to silicon alkoxides with the hydroxyl groups around the central silicon swapped for metoxyl or etoxyl groups.

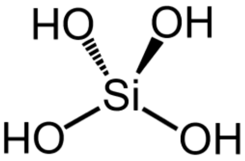

Figure 2-2: Hydrated ortho-silisic acid, the gel precursor.

To form a sol from the solution the SA must undergo a polycondensation reaction. We may add a catalyst, either a base or an acid, to control the rate [3]. The initial sol step of the sol-gel synthesis is the nucleation and growth of silica colloids from SA, the condensation reaction is shown below:

$$2Si(OR)_4 \rightarrow (RO)_3Si - O - Si(OR)_3 + R_2O$$

The condensation chains the SA molecules together along all four silanol groups forming the colloid for the sol. The by-product of the reaction is simply water, as opposed to ethers from alkoxides. After the sol has formed the colloids will aggregate together forming the gel. The colloids bind strongly to one another by the same condensation reaction shown above causing neck-formation [3].

It is this aggregation of colloids that give rise to the final gel microstructure, and it may change greatly depending on the synthesis parameters. Most important for us is the pH, considering that we will use acids or bases as catalysts during the reaction.

At high pH the colloids will tend to aggregate into small beady clusters due to a high cross-linking factor, then into larger chains [3]. The resulting microstructure looks remarkably like strings of pearls [13], as seen in figure 2-3. The open space between the chains form the larger mesopores, sometimes macropores, while the tiny crevises between and inside the beads formed by the colloids give rise to the micropores.

At low pH the colloids branch out more easily forming linear strings [3] in a denser microstructure as seen in figure 2-3. The space between the chains are smaller than for the high pH scenario giving a smaller average pore diameter, though the total pore volume does not nessesarily go down. The lack of bead-like aggregates causes the chains to be smoother and thinner, and this results in a fragile gel [14] that may suffer more shrinkage during drying.

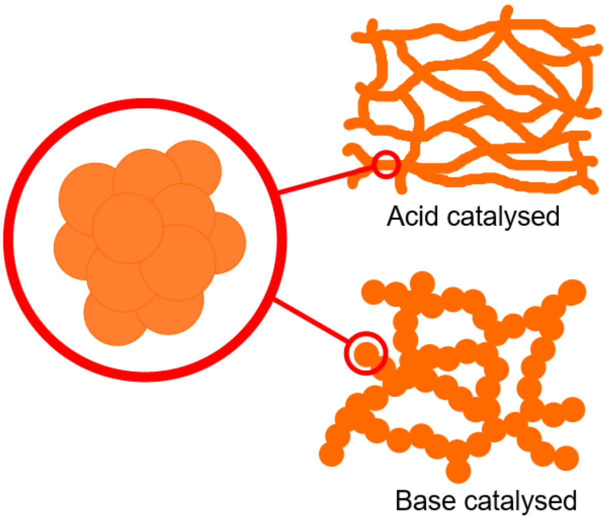

Figure 2-3: The differing gel structure resulting from acid or base catalysis of the sol-gel step.

We will use base catalysis for our synthesis as the base catalysed gels are both strong and hosts consistently large pore volumes with several micropores. The co-precursor method used also allows more easily for base catalysis, rather than acid catalysis. Gelation also tends to occur at a slower rate for low pH values [14].

Once the hydrogel is formed we must remove the water from the pores, and simply evaporating it off is not an option. Due to the surface tension between water and silica this will cause the entire structure to collapse in on itself. This process is called shrinking, and is to be avoided. If an aerogel shrinks completely, all mesopores will collapse and only micropores will be left. This material is known as a xerogel.

Avoiding shrinkage can be done in several ways. One such way is aging. By letting the hydrogel (or alcogel) sit for a time we allow the bonding between colloids to strengthen and rearrange. Final gel quality can be greatly increased by letting the hydrogel sit for a while, but not too long. A long aging process may smooth out micropore features, and if the pore water has a high pH the gel may partially dissolve, loosing its consistency.

2.3.2 Surface modification and drying

To make the move from hydrogel to aerogel we must remove the porewater from the hydrogel. Unfortunately, the surface of silica is covered in silanol groups, and this makes the surface very hydrophilic. If we were to put a silica hydrogel into an oven to evaporate the water away, the surface tension high surface tension between water and silica would collapse the gel completely.

To circumvent this problem and avoid shrinkage we typically use SCD with CO_2. Since supercritical fluids have no surface tension it can preserve the gel structure almost perfectly. The APD method requires surface modification of the hydrogel and solvent exchange before drying. The purpose of this is to decrease the interfacial tension of the pore-fluid and silica. Even then there is a severe chance of shrinkage unless we achieve a high degree of surface modification. This is achieved by way of the co-precursor method [4, 5].

The surface modification is done with silylation reagents, more specifically hexamethyl disiloxane and hexamethyl disilazane, or HDMSO and HMDS respectively [5]. These two chemicals react with the hydrophilic silanol groups and exchanges -H for $-Si(CH_3)_3$, a hydrophobic silyl group [5, 14], seen in figure 2-4. Figure 2-5 shows the molecular structure of the silylation reagents.

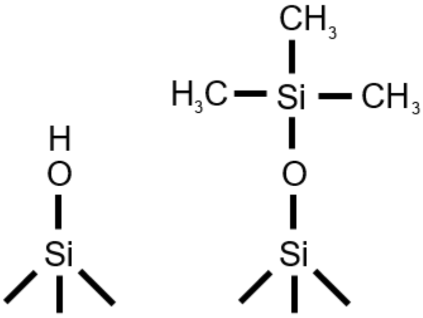

Figure 2-4: On the left, a hydrophilic silanol group. On the right, a hydrophobic trimethyl silyl group.

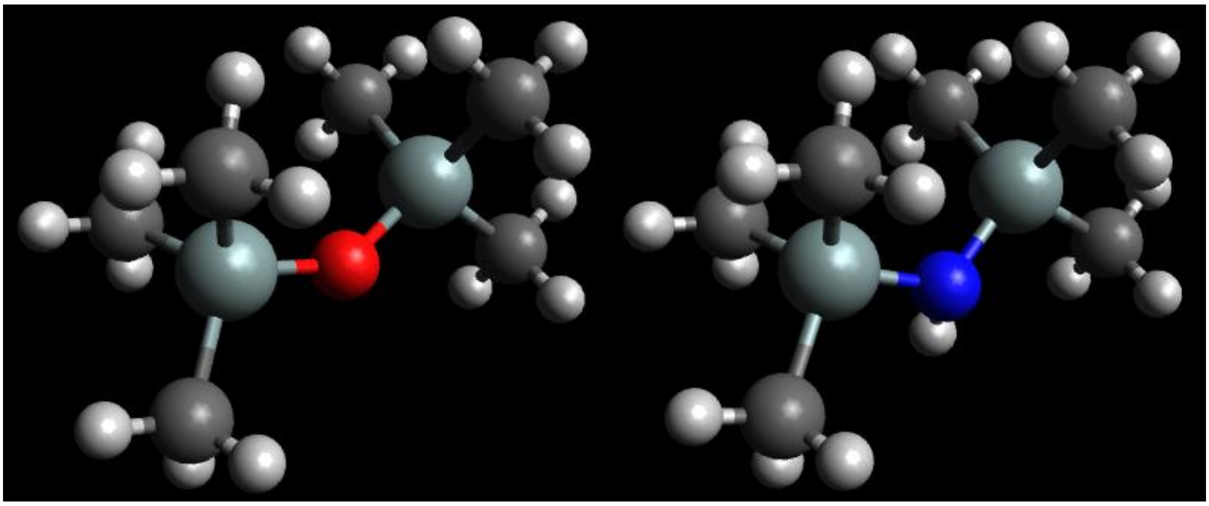

Figure 2-5: Silylation reagents, HMDSO on the left, HMDZ on the right. Hydrogen, carbon, silicon, oxygen and nitrogen are white, black, grey, red and blue respectively.

These reactions, shown below, also forms water or ammonia as by-products during the substitution. The first reaction is silylation by HMDSO forming water, the second is HMDS forming ammonia.

$$2Si - OH + O(Si(CH_3)_2 \rightarrow\ 2 \equiv Si - O - Si(CH_3) +\ H_2O$$

$$2Si - OH + HN(Si(CH_3)_2 \rightarrow\ 2 \equiv Si - O - Si(CH_3) +\ NH_3$$

There are several other silylation reagents available for use, and trimethyl chlorosilane (TMCS) is particularily effective [3, 4, 14, 16]. Kristiansen uses a synthesis tailored for incorporating copper ions and chose to use HMDSO and HMDZ which led to both high porosity and metal loadings [5].

Because the surface is now hydrophobic, we can exchange the water for a non-polar solvent, such as heptane, by covering the gel in the new solvent. As shown in figure 2-6 the water will be expelled from the pores as the surface becomes increasingly hydrophobic, the non-polar solvent enters the gel to replace the water. The process takes several hours leaving the pore-water as a separate phase. The time also allows the gel a chance to age as the solvent exchange occurs, though the process stops once the water is expelled.

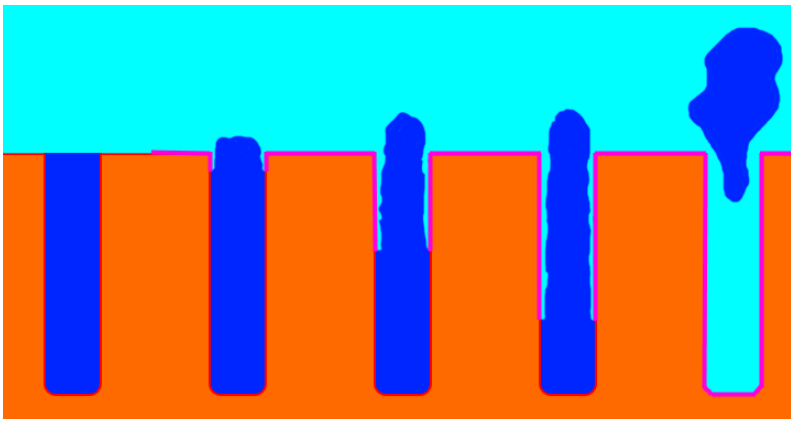

Figure 2-6: From left to right, a sequence of images showing a water filled pore growing increasingly hydrophobic. The hydrophobic pore eventually expels the water in favour of the outer non-polar fluid.

The surface modification step is usually very time consuming, especially if the silylation reagents are forced to modify the gel from the outside in. This is the case for the derivatization method where hydrogels are lowered into non-polar solutions of silylation reagents [4]. The co-precursor method is far superior, and adds the silylation reagents directly to the precursor solution at the sol-gel step [4, 5]. This causes the surface modification to happen from the inside out as the silylation reagents are already inside the pores. Overall the co-precursor methods lead to a higher degree of hydrophobicity [17], which decreases our chances of shrinkage during APD.

The silylation reagent HMDZ also serves a second role in this synthesis. HMDZ produces ammonia upon reaction with silanol, and it is this ammonia that will catalyse the sol-gel polycondensation [5]. Thus, the pH is determined in large part by the HMDZ content, and the HMDSO:HMDZ ratio can be used to control pH.

Lastly it is worth noting that HMDSO and HMDZ are non-polar and are not miscible in water. As such it is necessary to stir vigorously to start the sol-gel reaction upon adding the HMDZ. Stirring should continue until gelation to ensure a good dispersion of HMDSO and HMDZ throughout the gel.

2.4 Iron incorporation

Introduction of iron, or any d-group metal, to a silica aerogel matrix can be done in several ways. We intend to do an introduction of Fe^{3+} ions into the silica matrix itself as single sites. If this is done successfully, we expect to see one of two cases; the first is isomorphic substitution, where Fe^{3+} replaces silicon and ends up tetrahedrally coordinated. The second possibility would be that Fe^{3+} creates a new site geometry different from the tetrahedral silicon sites, most likely octahedral.

Iron is well known for inhabiting both tetrahedral and octahedral sites in several minerals and materials [18, 19], and the amorphous silica should allow deviating site geometry more than crystalline materials. As such, neither scenario is too unlikely.

Iron interstitially incorperated into silica frameworks are usually tetrahedrally coordinated for Fe^{3+} ions [20-22], while Fe^{2+} prefers octahedral coordination [22]. Even Fe^{3+} can appear octahedrally in oxides [18], oxide-hydroxides [23-25], aqueous complexes [25]. It has been shown that Fe^{3+} may interact with silica surfaces to form complexes with silanol groups, both octahedral [25] and tetrahedral [26] may be possible. Precipitation of iron hydroxides may form grafting of small octahedral clusters [25] of oxide or oxide-hydroxide.

Figure 2-7 shows a possible tetrahedral structure at the surface. This is perhaps our best case scenario with surface available Fe(III) single-sites strongly bonded to the silica. As the silica matrix is amorphous we would also expect some distortion of the site geometry. It is not unlikely that the iron atoms will be available from the surface either, as copper atoms incorporated by the same method produced surface active single sites [5-7]. Fe^{3+} ions are known to form complexes with silisic acid [27, 28], the penultimate precursor to the silica gel by our synthesis route. This may help incorporate the ions into the silica structure despite Fe^{3+} tendency to form small hydroxide clusters and precipitate [22, 25].

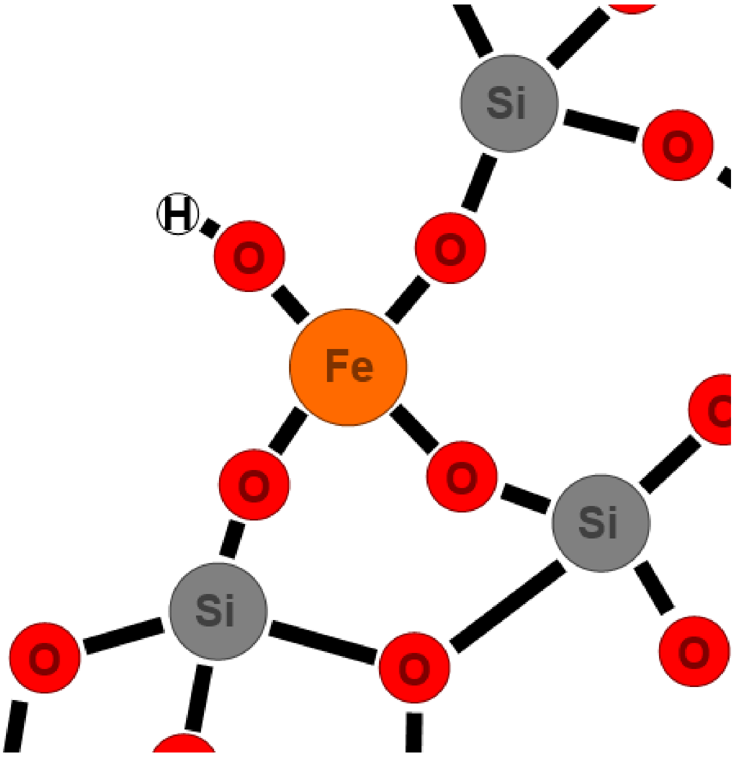

Figure 2-7: Possible result of iron incorporated into a 4-coordinated tetrahedral site in amorphous silica. One coordinated oxygen terminating in a surface hydroxyl group.

Due to iron(III) nitrate being our precursor there will most likely be a bias towards Fe^{3+}. Some authors hypothesise that Fe^{3+} may reduce to Fe^{2+} as we burn off surface modifying groups creating a reducing environment [29]. Fe^{3+} is still quite stable as a precursor, and unlikely to be reduced during synthesis [30], in fact it is Fe^{2+} that usually oxidizes in favour of Fe^{3+} during sol-gel reactions [31, 32]. Since the removal of surface modifying groups also occurs in an oxygen atmosphere Fe^{2+} is considered unlikely, and Fe^0 more so.

In the event that iron single sites do not form, we expect the formation of small Fe_xO_y particles. These particles may be small nanoparticles perhaps confined to the micropores or larger particles or particle clusters deposited in the mesopores, perhaps both. Their composition may be similar to iron oxides, iron hydroxides or iron oxide-hydroxides. The most notable Fe^{3+} bulk compounds that we will discuss are the iron(III) oxides hematite and maghemite, as well as the oxide-hydroxide ferrihydrite. Also magnetite, containing both Fe^{3+} and Fe^{2+}.

For the oxides hematite contains only octahedral Fe^{3+} sites while maghemite contains 37.5% tetrahedral sites [23]. Maghemite is also ferrimagentic due to its crystal structure. Ferrihydrite is an extremely common form of ferric oxide-hydroxide that form readily in nature, but the exact structure is largely unknown [23, 24]. It is hypothesized to contain both octahedrally and tetrahedrally coordinated Fe^{3+}. Magnetite is a black, ferromagnetic mineral containing octahedrally coordinated Fe^{2+} ions and both tetrahedrally and octahedrally coordinated Fe^{3+} ions.

There has been several previously reported attempts at loading silica aerogel with d-group transition metals such as cobalt [33], vanadium [34], copper [5, 34] and indeed iron [29, 30, 35, 36]. The main difference is that many of these attempts use commercially unviable methods or precursors like the silicon alkoxides and SCD. Of the attempts at incorporating iron Jitianu et Al., Casula et Al. and Fabrizioli et Al. all report for iron oxide particles rather than single sites [29, 30, 35]. Popovici et Al. utilizes impregnation [36], a method that generally grafts ions loosely to the surface.

To the best of the authors knowledge, Kristiansen et Al. [5] is the only researcher to document a commercially viable synthesis route developed for transition metal ion incorporation. So far, the route has proven successful at generating copper single-sites and it is our goal to test the effectiveness of this method for other metals. Iron is chosen due to the interesting chemistry of iron single sites, as they are now hypothesized to show increased activity for methane activation [10, 11]. Even iron-silicates and supported iron oxide particles are interesting as catalysts [37].

Iron(III)nitrate is our precursor of choice due to three reasons: It is cheap and readily available. Kristiansen herself utilized nitrate or acetate salts [5]. Lastly, Fe^{3+} are stable and known to form complexes with SA [27, 28].

2.5 Colour of iron compounds

Due to being a transition metal iron is associated with colourful chemistry. The colour of the final product may help to determine the nature of the iron species. Figure 2-8 shows a variety of iron(III) compounds and their colour.

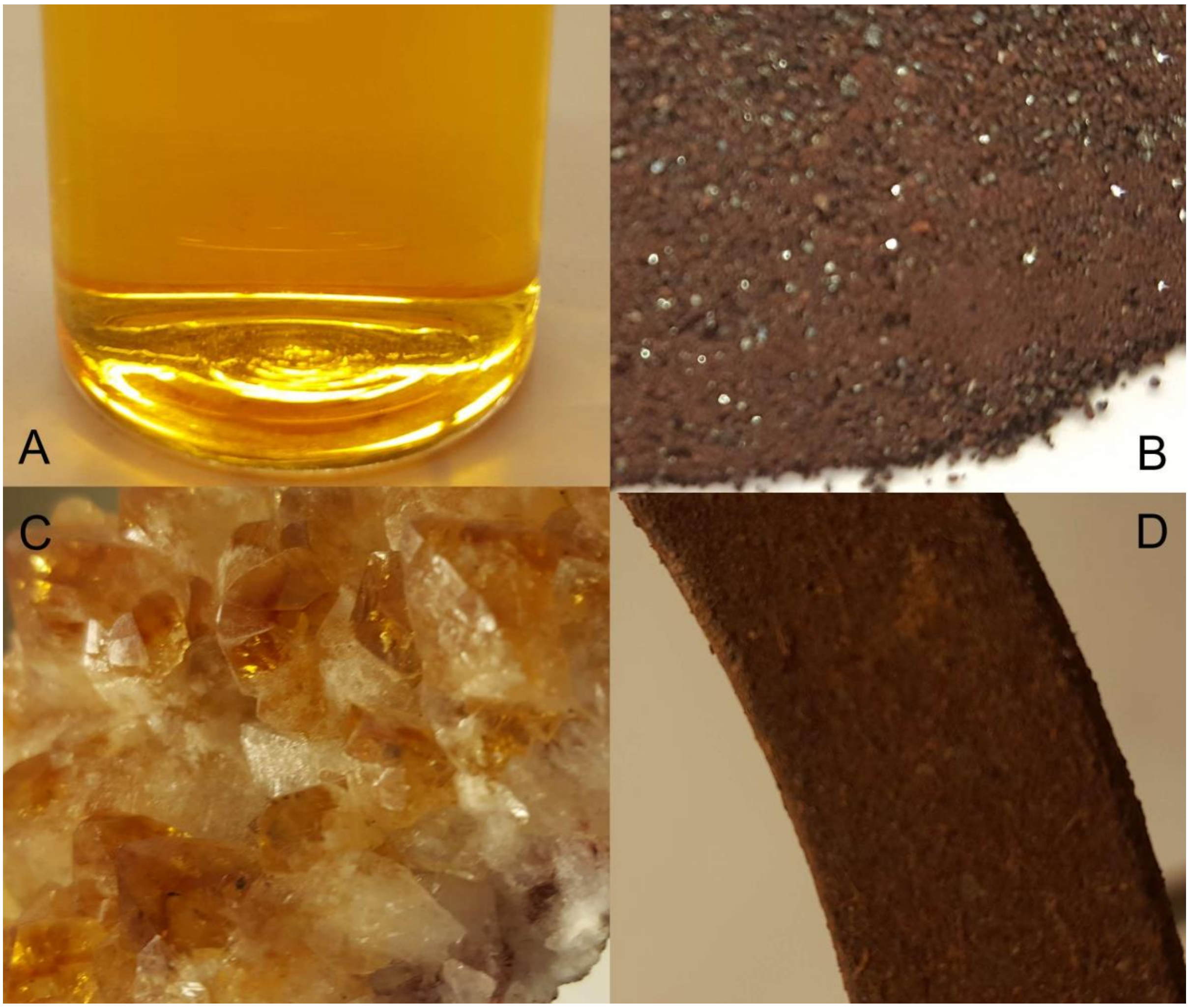

Figure 2-8: Various compounds containing iron(III). A: An aqueous solution of iron(III) nitrate. B: The Iron(III) oxide hematite. C: Naturally occurring citrine, quarts containing iron(III). D: Common rust.

Figure 2-8A shows a solution of iron(III) nitrate, the precursor used in our synthesis. It is clear yellow-orange with colour intensity dependent on the concentration. The colour arises from charge transfer transitions in the blue end of the visible spectrum, which we will discuss later. At higher pH small FeOH clusters will precipitate [32], darkening the solution to dark orange or brown. Figure 2.8B shows hematite, a quite stable iron(III) oxide. Hematite is quite different from the solution, the colour being much darker brown with a tinge of purple.

Figure 2-8C shows citrine, a naturally occurring variant of quartz containing Fe^{3+} impurities. The colour of this gemstone is very similar to the solution above, and its colour is derived from nano-clusters of Fe_2O_3 as well as interstitial single sites [22]. The rust shown in figure 2-8D is more complicated. Rust is a combination of several iron(III) compounds like ferrihydrite and hydrated iron oxides. The colour of rust varies from orange to nearly black.

While figure 2-8 presents citrine as orange it can also occur as a light yellow [38]. This colour is quite unusual for iron compounds, as most others are red or black. Magnetite and hematite, for example, are black minerals in bulk[38]. Hydrated oxides and oxide hydroxides tend to form red colours [38]. Yellow is then associated with single sites, while oranges should indicate larger particles. Brown would indicate hydrated compounds and black indicates dry oxides.

2.6 Characterization

The finished aerogels must be characterized to determine whether they are indeed aerogel materials, whether they contain iron and whether the iron is in a single site environment. The methods used range from routine techniques like XRD to more powerful techniques like XAS, which will be covered in more depth.

2.6.1 X-ray diffraction

XRD is a technique for determining crystal phases. Monochromatic x-rays are fired at the sample at certain angles θ and scattered by the crystal structure. The intensity of the outgoing x-rays are measured at the same angle. By varying the angle we create a diffractogram. The diffractogram functions as a crystallographic fingerprint unique for every crystal system [15].

Silica aerogels, being a product of the sol-gel synthesis, are not crystalline. The diffractogram for an amorphous powder has no diffraction peaks, as there are no repeating planes in the lattice. Should our samples be single-site iron in silica aerogel we would expect them to still be amorphous, as single sites would not give long-range order.

Should the diffractogram show signs of crystallinity this will be due to either the silica being crystalline or due to crystalline iron species. In either case we can use the diffraction pattern to determine the exact compound and crystal structure assuming a match exists in the database.

We can also use XRD to detect changes to the crystallinity before and after annealing the material. We can see if our material loses or gains crystallinity or if it changes its crystal structure completely. This is useful for determining the stability of the finished product. The synthesis may provide single-sites, but if annealing causes iron to leave these sites in favour of a large crystalline oxide phase, it will be visible in XRD.

Should there develop large iron species in the silica aerogel, XRD will detect it, but smaller particles may be problematic. Very small crystalline particles will cause peak broadening until they eventually disappear. This can be mitigated by increasing the x-ray energy. Higher energy x-rays will lower the levels of noise making even broader peaks visible. The exact size limit is difficult to determine, but it is definitely within the nano-scale [15].

2.6.2 Nitrogen adsorption/desorption isotherm

Nitrogen isotherms are used to probe the surface of a sample material. The isotherm itself is merely a measure of nitrogen physisorbed to the sample surface as a function of relative pressure. The measurements can be done over a small or large range of partial pressures depending on the data we want to collect. For some measurements it is necessary to plot one line for adsorption and desorption separately as they may deviate from one another. These are called the adsorption and desorption curves.

The nitrogen isotherm can appear different depending on the material probed; Sing et Al. mentions six types of isotherms [39], but we will focus on the three most common shapes as shown in figure 2-9.

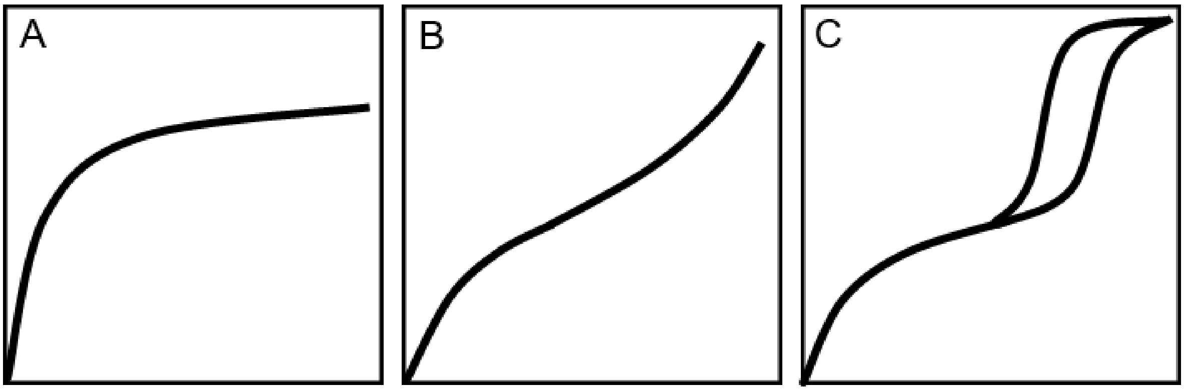

Figure 2-9: Three types of isotherms. A: microporous solid with limited surface area. B: nonporous or macroporous solid allowing unrestricted layer monolayer-multilayer formation. C: Mesoporous solid with hysteresis loop formed by capillary condensation.

Figure 2-9A is typical for a microporous material with limited surface area, and thus limited room for adsorption layer formation. After the adsorption of an initial monolayer the curve evens out considerably. This is also known as a type I isotherm [39].

Figure 2-9B shows the isotherm for a non-porous or macroporous material. The convex shape after the initial monolayer shows unrestricted growth of additional layers. This is also known as a type II isotherm [39].

Figure 2-9C shows the expected isotherm for a mesoporous material. By far the most distinctive feature is the hysteresis loop where the adsorption (bottom) and desorption (top) curves deviate. This is due to capillary condensation during adsorption. During desorption the condensed adsorbent is more difficult to remove and persists at lower partial pressures. This is also known as a type IV isotherm [39].

The shape of the hysteresis can also change, and this seems indicative of the pore shape. The ideal hysteresis shape for silica aerogels is a long, slender and sometimes almost horizontal shape. This indicates long and slit-like pores but also hints at the existence of micropores [39]. This is also similar to the isotherms detected by Kristiansen and other waterglass aerogels [4, 5].

Nitrogen isotherms conducted at 77 K are good at measuring micropores, but we can still detect them [39, 40]. The method is particularly well suited for measuring mesopore distributions [40], which makes it well suited for our purposes. For macroporous materials other methods are recommended [39].

We can gain a lot of information from analysing the isotherm as is, but it can also be analysed mathematically. Using various methods we can calculate specific surface area, average pore size and pore size distribution to mention a few. This is done primarily through BET theory and BJH theory.

Brunauer-Emmet-Teller theory

The BET theory was developed by Brunauer, Emmet and Teller in 1938 [41], and is a method for measuring specific surface areas. The method itself is based on the BET equation shown below. This equation is based on multilayer Langmuir adsorption, and predicts a linear isotherm that is mostly applicable at low relative pressures. At this range most mesoporous isotherms are generally linear. The BET equation looks like this:

$$\gamma = \frac{1}{n(\frac{p_0}{p} - 1)} = \frac{C-1}{n_{mono}C}\frac{p_0}{p} + \frac{1}{n_{mono}C}$$

Where n is the amount of adsorbed nitrogen, p is the partial pressure, p_0 a reference pressure, C is the BET constant and n_{mono} is the amount of adsorbate needed for a monolayer covering.

The BET constant C is dependent on heat of adsorption and heat of condensation. From the BET equation we can eventually calculate the specific surface area, SSA or A_{BET}, by constructing a BET plot.

Due to the distortion of the isotherm caused by micropores at low partial pressures (figure 2-9A), BET is not a good method for micropores and may over- or underestimate the true SSA value. BET theory invokes many approximations and cannot always be trusted, but otherwise, it is a quick and easy technique for measuring surface area.

Barret-Joyner-Halenda theory

Barret, Joyner and Halenda developed BJH theory in 1951 [42], but although there is a BJH equation BJH analysis now refers to a wide range of methods, all related to the original [40]. Compared to the relatively simple BET method BJH requires many data points throughout the adsorption and desorption curves, and is developed for calculating the pore size distribution of mesoporous materials [40]. BJH has the same problems with micropores as BET.

Combining all methods of BET and BJH we can calculate several important parameters for our samples. SSA is not too important as it may indicate a rough surface as well as porosity. Pore volume, V_p, is perhaps the most important for aerogels as they are in part defined by their porosity. Average pore size, D_p, is particularly useful in combination with the pore size distribution, and we can estimate the relative population of small and large pores.

2.6.3 Inductively coupled plasma mass spectrometry

ICP-MS is an extremely sensitive qualitative analysis method that ionizes a sample using plasma and measures elemental content by weight. The apparatus can measure nearly all elements in the periodic table, with the exception of those used to prepare and/or dilute the sample beforehand or otherwise introduced from the instrument. This includes for example hydrogen, oxygen, fluorine and nitrogen from water and acids or argon from the plasma torch etc. The results gained by ICP-MS are usually accurate enough to detect 1-10 ng in one liter of solution and is widely used for analysing metal content [43].

The method is destructive and requires dissolving the sample in digesting acids. Silica aerogels are digested in hydrofluoric and nitric acids before diluted. The apparatus is extremely sensitive and requires the sample to be extensively diluted, thus the largest errors are from impurities introduced during preparation or errors in dilution. In short, ICP-MS is an exact and trustworthy technique capable of pinpointing the iron content of our samples with unparalleled accuracy.

2.6.4 UV-vis absorption spectroscopy

UV-vis refers to absorption spectroscopy using wavelengths of light in the ultra violet and visible region. Photons in this energy range are produced by a source, filtrated to one wavelength and then exposed to the sample. The intensity of this monochromatic beam is measured by detectors both before and after encountering the sample, and the difference corresponds to the samples absorbance for that wavelength. Allowing the filter to scan across all wavelengths produces an absorbance spectrum. For solid, opaque powder samples like aerogels the light beam is reflected off the sample. For clear liquid samples we would transmit the beam through the sample instead. Figure 2-10 shows a simplified schematic.

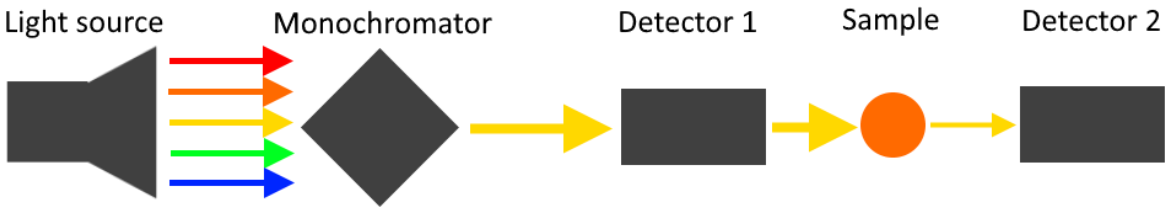

Figure 2-10: The general setup for absorption spectroscopy.

The energy of the light used in UV-vis is in the range of electronic transitions for valence electrons. An absorbance in the UV-vis range equates to an excitation of a valence electron, and the energy of the absorbance is the energy difference of the initial and the excited state.

The theory used for explaining these absorptions is the ligand field theory. Ligand field theory regards electronic energy levels as molecular orbitals (MO) formed by symmetry allowed linear combination of atomic orbitals (AO). The MOs are then filled by the valence electrons of all contributing atoms, shared MOs forming bonds and unshared MOs forming lone pairs. Ligand field theory is usually adapted for metal complexes with a central metal atom and surrounding ligands, but it is also applicable to metal oxides where the coordinating oxygen atoms function as ligands. For transition metals like iron there are three UV-vis active transitions: The d-d transitions, ligand to metal charge transfer (LMCT) and metal to ligand charge transfer (MLCT) [44].

The so-called d-d transitions are actually transitions to and from MOs mostly belonging to the central atom, and their main contributing AO are the d-orbitals. d-d transitions are thus transitions taking place at the central atom itself between MOs with mostly d-type character. The charge transfer (CT) transitions are transitions where the excited electron transfers between central atom-type MO and ligand-type MO [44].

The requirements for d-d transitions is a central atom, specifically an ion, with at least one available d-type valence electron. There also has to be less than 10 such electrons for there to be an available final state. CT transitions require either specific ligands or oxidation states. MLCT, for example, is facilitated by either ligands with low energy lone pairs or central atoms with low energy empty states. MLCT is usually observed in high oxidation state metals coordinated by O^{2-} ligands [44].

Absorption peaks have primarily two features: Energy, or position and intensity, or height. The energy is decided by the energetic gap between the initial and final state. The intensity is a measure of how likely the transition is. The likelihood of transition is predicted by the transition selection rules.

The spin selection rule states that transitions between two states with the same spin function are forbidden. In practice some spin forbidden transitions will occur, but their intensity are always very low. The laporte selection rule states that for centrosymmetric systems only transitions accompanied by a change in parity are allowed. The result is that d-d transitions in a perfect octahedral complex would be forbidden as both the initial and final state has the same parity, but for tetrahedral systems the rule does not take effect. Laporte forbidden transitions occurs in practice due to vibrations and imperfect symmetry in the coordination, and have a noticeable intensity larger than the spin forbidden transitions. CT transitions have very large intensities compared to even spin and laporte allowed d-d transitions [44].

The Iron Spectrum

Iron is a 3d transition metal with a $4s^2\ 3d^6$ electron configuration. It is normally stable at three oxidation states, metallic Fe and as the cations Fe^{2+} and Fe^{3+}. Fe^{2+} has a d^6 configuration and Fe^{3+} has a d^5 configuration. Studies of iron silicates, including in silica gel environments, show that oxygen is the coordinating ligand, as well as the possibility of tetrahedral and octahedral iron in single sites and oxide clusters [29-31], so these are the possibilities we will consider. In both the tetrahedral and octahedral scenario Fe^{3+} has a high spin configuration, meaning d-d transitions are spin forbidden [18, 45].

In the absence of d-d transitions most spectra of Fe^{3+} in solution are dominated by a CT feature between 200 and 300 nm [32, 45] and indicates solitary iron [46]. The CT feature is usually resolved as two distinct peaks, their exact position dependent on ligands and coordination. Tetrahedrally coordinated iron tends to form two CT peaks at roughly 215-220 nm and 240-260 nm [20, 47], whilst octahedrally coordinated sites are more redshifted towards 280-290 nm

[29]. If these distinct CT peaks are difficult to distinguish it may be a sign of mixed sites or sites of low symmetry [46].

A CT peak at 300 nm and beyond is reported to indicate Fe-OH [32], and the broadening of this peak towards larger wavelengths, causing the formation of a tail feature, indicates larger particles of oxide or hydroxide [32, 46]. Should this tail feature broaden to 350-450 nm it indicates the existence of considerable colloids [32], and at 500-550 nm larger oxide/hydroxide particles [47]. Depending on the ligands the d-d transitions may be visible, although weak [29, 31].

Interpreting the iron spectrum is rather difficult. The various CT peaks vary depending not only on coordination but also on the ligands. Many overlap or exist in the same region and the literature does not always agree on the origin of the features. The simplest things to look for are the CT feature at the low wavelengths indicating solitary sites and the redshifted shoulder beyond 300 nm implying precipitated colloids and oxides [32, 45]. Beyond this, specific conclusions can be difficult to draw.

2.6.5 X-ray absorption spectroscopy

XAS is structural characterization technique that probes individual atoms of a given type. It is non-destructive, applicable to solids, liquids and gases both ex and in situ. It can give information about oxidation state and chemical environment several ångstrøm from the probed atom. It can probe for virtually any type of atom, but the energy requirements vary depending on the atom type. These energy requirements for the x-rays makes XAS exclusively a synchrotron technique, and this is probably the biggest downside to an otherwise powerful characterization tool. Another downside is that it averages the results over all atoms probed, and this must be taken into account during analysis. [48, 49]

XAS is a form of absorption spectroscopy, and on the surface it may seem similar to UV-vis. The setup for XAS is very similar to figure 2-10, but the light source is a synchrotron producing high energy x-rays [49]. The theory behind absorption is also different from the low energy UV-vis photons. The absorption coefficient μ is larger for denser materials with large atomic nuclei, but it also depends on the x-ray energy [48]. The approximate formula for μ is shown below.

$$\mu \approx \frac{\rho Z^4}{AE}$$

Where A is the atomic mass of the sample, Z is the nucleic charge, ρ is the density and E is the x-ray energy. The general trend is that higher energy x-rays are absorbed less frequently, but this trend is broken at certain energies by features called absorption edges.

An absorption edge is the ionization of a core state electron, such as a 1s, 2s or 2p electron. At the required energies these ionizations form sharp increases in the μ(E) spectrum (figure 2-11). Every atom has absorption edges at specific energies, the highest energy being the 1s ionization, or the K-edge. For higher energies the second shell electrons create L-edges (several exist) followed by M-edges for the third shell etc… Before each absorption edge there may be a smaller feature called a pre-edge. The pre-edge is an excitation of the same core-state electron to a partly filled valence state [48].

The XAS spectrum is a plot of μ(E) and is divided into two regions: The X-ray Absorption Near Edge Spectroscopy (XANES) region, and the Extended X-ray Absorption Fine Structure (EXAFS) region (figure 2-11). These two regions gives information about the target atom, but in different ways, and are interpreted separately.

X-ray absorption near edge spectroscopy

The XANES spectrum encompasses a relatively short part of the total spectrum, and the most prominent feature is the main absorption edge. This edge corresponds to ionizing the target atom by removing a core electron. As an example, the XAS spectrum of an iron metal foil standard is shown in figure 2-11.

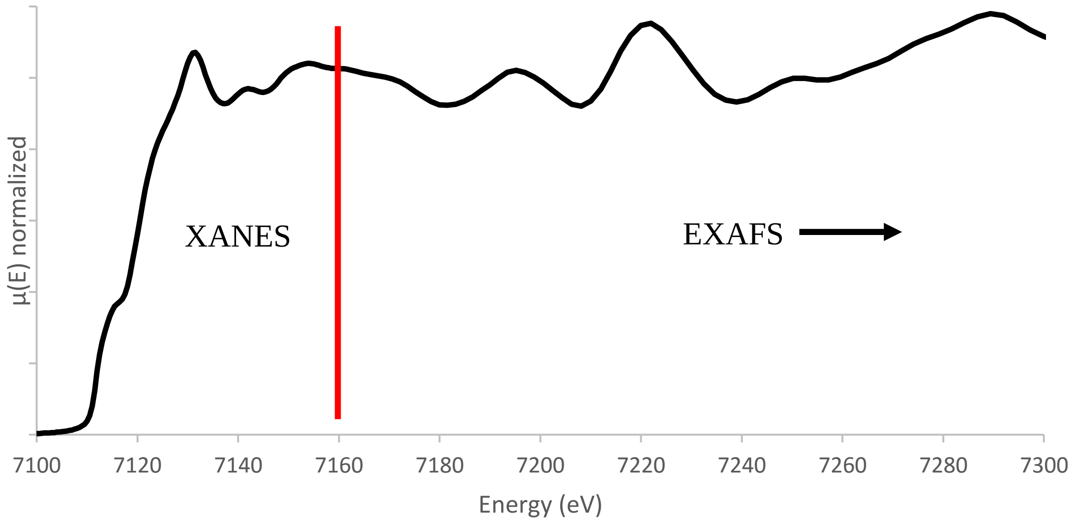

Figure 2-11: XAS spectra of iron metal foil at the K-edge. XANES is the regime up to 7160 eV, EXAFS is everything beyond and is only partially shown.

The position of the K-edge for iron metal is defined as the first maxima in the first derivative of μ(E). This value is 7112 eV [50], and is used to correct for energy shifts in the instrument, and when comparing data with other authors who might use other values [18, 19]. Once the iron metal K-edge is positioned correctly we can measure other compounds. The position of the absorption edge for all other compounds is measured as the energy where μ(E)=0.5 for the normalized spectrum. The position of the K-edge changes depending on oxidation state [18], and using known standards allows us to estimate the state for unknown samples as well as correct for energy shift by the instrument. Some other information, like coordination, ligand bond length and symmetry of the sites can also be discerned to some degree, as they are implied by the shape, size and position of the edge-crest feature [51].

In front of the K-edge we may also observe a solitary peak formation called a pre-edge feature, although for iron metal this appears more like a shoulder in the absorption edge. The pre-edge is the excitation of the 1s electron to a valence state. This follows the same general rules as UV-vis d-d transitions in terms of selection rules and position being dependent on the transition energy.

The Fe-K pre-edge is a 1s-3d transition meaning it is Laporte forbidden for centrosymmetric iron atoms. The intensity of the pre-edge is thus indicative of coordination with tetrahedral sites having larger intensities than octahedral ones, 5-coordinated iron falling in-between [18].

General level of symmetry may also play a role. The position of the pre-edge is also influenced by the oxidation state and can be used in conjunction with the K-edge position [18, 19, 52].

The pre-edge may also be a combination of two or more transitions. This is due to energetic splitting of the d-orbitals. An octahedral field will cause the d_{x2-y2} and d_{z2} orbitals to become less energetically favourable due to overlap with the ligands orbitals. The d_{xy}, d_{xz} and d_{yz} orbitals more energetically favourable to compensate. Since the d-orbitals are no longer degenerate, we observe two excitations very close to one another. Tetrahedral field cause the opposite splitting, and the splitting energy for tetrahedral fields (Δt) is not as high as that for octahedral fields (Δo) [44]. Octahedral Fe^{3+} would give two overlapping pre-edge features due to these two 1s-3d transitions. Tetrahedral Fe^{3+} would do the same, but since $\Delta t = 4/9\Delta o$ the splitting would be smaller and hard to notice [52]. Multiple pre-edge features may also indicate a mixing of oxidation states [18, 52].

Extended x-ray absorption fine structure

The EXAFS part of the XAS spectrum is very large compared to the XANES region, extending far beyond it. It is also interpreted in a very different way and gives information on the target atoms surroundings. When analysed properly EXAFS gives us the distance, identity and number of neighbouring atoms in concentric "shells" around the target atom. The distance we can see beyond the central atom depends on the quality of the data. EXAFS is a very powerful tool for acquiring structural information of unknown samples [53].

The intensity of the μ(E) spectrum depends on the probability of transition, and a transition cannot occur if there is already an electron present in the final state. Any ejected photoelectron will propagate through the material as a wave and interferes with neighbouring atoms backscattering and then returning towards the central atom. The reflected wave now interferes with the final state, and thus affects μ(E) [48]. This is the origin of the fine structure in the EXAFS region of μ(E). The fine structure appears as waves and fluctuations in μ(E) after the absorption edge, as seen in figure 2-11, although it may be difficult to see in the μ(E) spectrum. To better see the effect of the backscattered photoelectrons we subtract the theoretical background absorption expected for a lone atom in the gas phase $\mu_0(E)$. We also divide by $\Delta\mu_0(E)$, the energy difference measured at the absorption edge. This results in χ(E) [48].

$$\chi(E) = \frac{\mu(E) - \mu_0(E)}{\Delta\mu_0(E)}$$

The Chi curve is not normally given as a function of the x-ray energy E, but rather the wavenumber k of the ejected photoelectron. The photoelectron has the energy left over from the ionization, so the absorption edge position E_0 becomes k=0.

$$k = \sqrt{\frac{2m_e(E - E_0)}{\hbar^2}}$$

Where m_e is the electron mass, ħ is plancks constant divided by 2π, E_0 is the absorption edge position and E is the x-ray photon energy.

This new χ(k) (figure 2-12) is a sum of sine waves, each one representing backscattering from a different coordination shell. This is given by the EXAFS equation below.

$$\chi(k) = \sum_j \frac{N_j f_j(k) e^{-2k^2\sigma_j^2}}{kR_j^2} \sin(2kR_j + \delta_j(k))$$

For all shells j, where N and R are the number of atoms and radial distance respectively. σ^2 is disorder of the distance R and is known as the Debye-Waller factor. f(k) is the scattering amplitude and δ(k) is the phase shift of the scattered electron, both are dependent of Z in the scattering atom [48]. The EXAFS equation can be expanded to more terms, but this simplified version shows most of the relevant parts [53, 54]

The EXAFS χ(k) curve is analysed by creating a theoretical curve which is then fittes to the experimental. The theoretical curve is based on the EXAFS equation, but contain only a few sine waves. Each sine wave represents a single fitted absorption shell. The identity of the atom at each shell is chosen manually, but software is then used to fit the other variables N, R and σ^2 [48]. The software also gives a fit-value that is used to determine how well our fitted function corresponds to the experimental χ(k). For high values of k the χ(k) signal grows very weak, and we multiply χ(k) with a weighing factor, usually k^n where n=1, 2 or 3 to amplify the signal at high k. An example of a $\chi(k)*k^3$ curve and a fitted function is seen in figure 2-12.

The χ(k) curve and the fitted functions can both be fourier transformed (FT). The FT curve shows the environment radially from the central atom with peaks and shoulders representing shells. An example of a χ(k) curve and the corresponding FT curve is seen in figure 2-13.

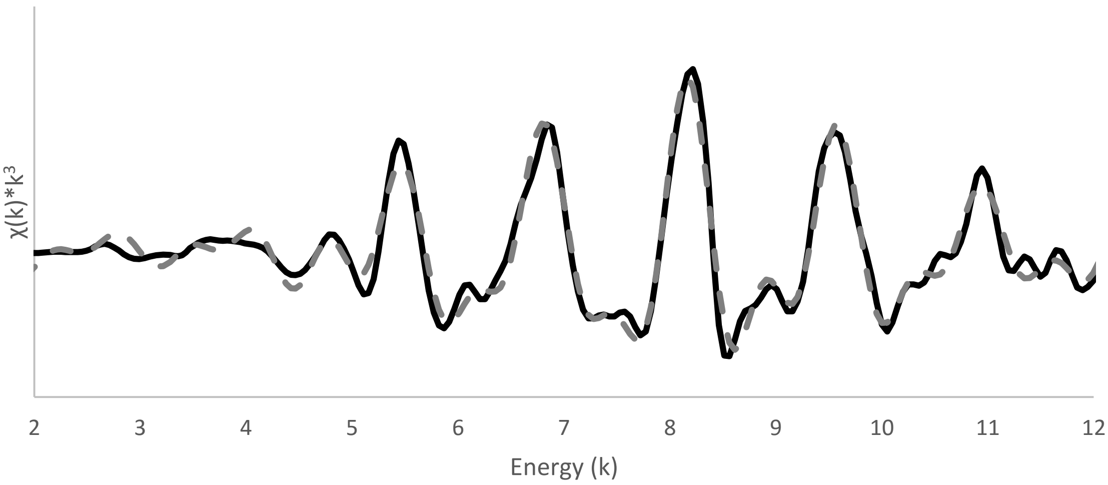

Figure 2-12: Chi curve for iron metal foil (solid) and a fitted line (dashed). k^3 weighted.

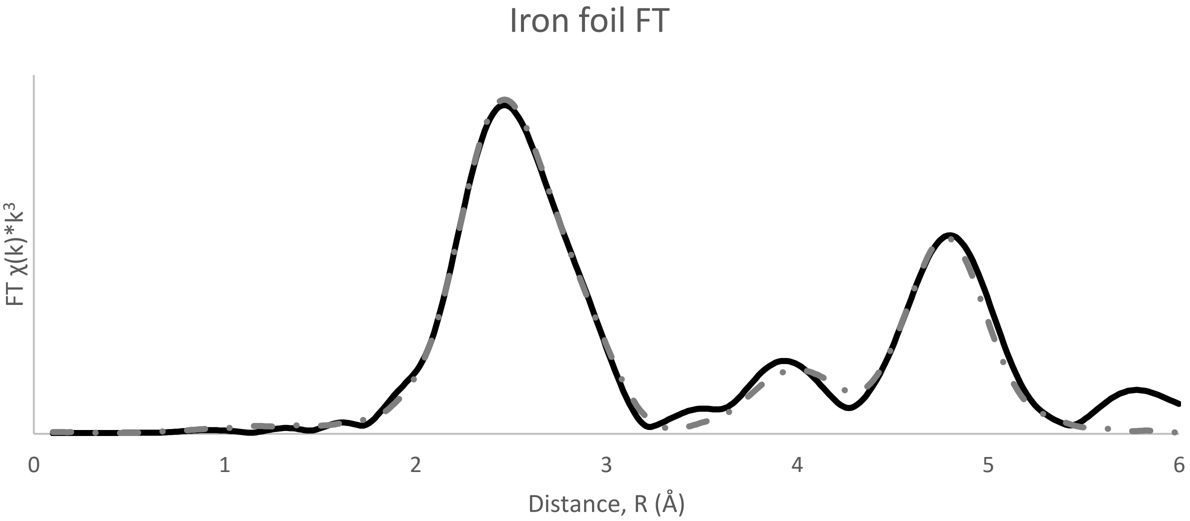

Figure 2-13: Fourier transformed χ(k) curve for iron metal foil (solid) and fitted line (dashed).

Fitting the χ(k) curve can be done without reference compounds, but the values for N may suffer. This is due to the fitted variables correlating. If one wishes to determine chemically relevant data one must fit a known compound with known multiplicities to calculate a variable called AFAC in the software EXCURV98. It is otherwise known as the amplitude reduction factor [54]. This value can then be used for unknown samples, though the known compound should be as similar to the unknown compound as possible.

Fitting the χ(k) curve is not simple, and a handy tool for fitting particularly difficult shells is fourier filtration. Fourier filtration isolates only a particular part of the FT curve, the shell we are interested in, and cuts everything else. The FT curve is then transformed back into a much simpler χ(k) curve. Fourier filtering can thus be used to fit shells one at a time. An example is shown in figure 2-14.

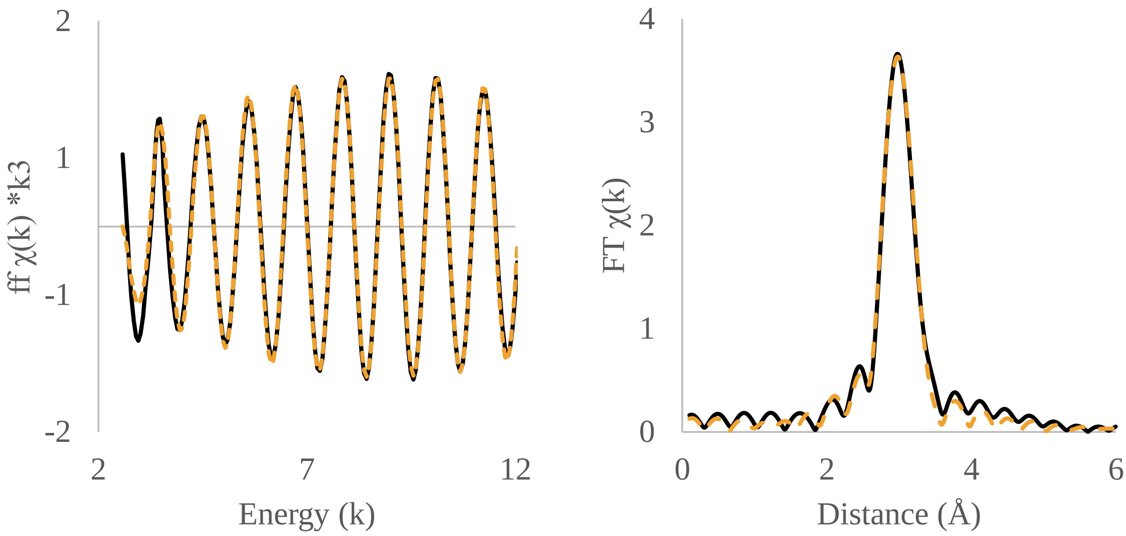

*Figure 2-14: Figure 2 14: Fourier filtered χ(k)*k^3 curve and FT curve. Data from sample FeAG7 filtered between 2.6 and 3.0 Å.*

3 Experimental

3.1Synthesis

The synthesis starts with a solution of sodium silicate (8 $_{w}$%). This solution was obtained by diluting sodium silicate (Sigma Aldrich, 29.5 $_{w}$%, 18 ml) in distilled water (47 ml). This solution was then ion exchanged by pouring it through a column of amberlite 120IR resin (Fluka Analytical). The result is a solution of silicic acid (SA) with a measured pH of 2-3.

The silicic acid was distributed into batches of 20 ml in small beakers. The metal precursor, $Fe(NO_3)_3 \cdot 9H_2O$ (Sigma Aldrich, 0.5 g, 1.0 g, 1.5 g etc..), was added and stirred until completely dissolved. The pH is lowered depending on the amount of Fe^{3+} as it is an acidic cation, sometimes lower than 1.

Each batch was set to stir vigorously as the silylation reagents were added to ensure thorough mixing of the two phases. First HMDSO (Fluka Analytical, 4.87 g) and then HMDS (Fluka Analytical, 4.84 g) in quick succession, but the HMDS was added carefully. Upon addition of HMDS the pH quickly increased and gelling started to occur. The stirring was vigorous enough that the two phases were mixed thoroughly until the gelling was complete. pH upon gelling was usually 7-9 and continued to rise to 8-9. The time required for the gel to form varied with iron content, but stayed under a minute.

The gels were transferred to larger beakers using ceramic spatulas and covered in heptane (source). Over the course of 24 hours the water phase was expelled as the surface modification progressed to make the gel more hydrophobic. At this stage the gels would float on top of the expelled water phase.

The heptane hydrogels were transferred to petri dishes after decanting as much of the water phase off as possible. A sample of the water phase was taken for analysis as well. The gels where dried in air at 65°C for 18 hours, 85°C for 3 hours, and 120°C for 2 hours with heating rate of 5 °/min between each dwelling step.

The finished samples were mortared and annealed as needed. Annealing was done at 450°C for 30 minutes, with a heating rate of 5 °/min.

3.2 Samples

The table 3-1 below shows a comprehensive list of all samples synthesized. Iron containing gels are named FeAG and plain silica aerogels are named PAG. The accuracy of these numbers vary as the SA content formed by the ion exchange is uncertain. This step also adds an unknown amount of water, so the reported numbers are estimated from the original waterglass solution.

Table 3-1: Summary of all samples synthesized and their synthesis parameters.

Sample	Batch	Molar ratio SA:H_2O:Fe:HMDSO:HMDS				
		SA	H_2O	Fe^{3+}	HMDSO	HMDS
FeAG1	1	1	41	0.07	1.67	1.57
FeAG 2	2	1	31	0.05	1.20	1.27
FeAG 3	3	1	30	0.06	1.13	1.13
FeAG 4		1	30	0.11	1.13	1.13
FeAG 5	4	1	24	0.08	1.00	1.00
FeAG 6		1	24	0.24	1.01	1.01
FeAG 7	5	1	27	0.04	1.05	1.07
FeAG 8		1	27	0.09	1.05	1.09
FeAG 9		1	27	0.13	1.05	1.05
FeAG 10		1	27	0.18	1.05	1.06
FeAG 11		1	27	0.22	1.06	1.06
FeAG 12		1	27	0.27	1.04	1.06
FeAG 13	6	1	28	0.17	2.09	2.11
PAG 1	1	1	41	0	1.66	1.57
PAG 2	3	1	30	0	1.13	1.13
PAG 3	6	1	28	0	2.09	2.09

3.3 Characterization

Simple visual inspections during synthesis help determine if the synthesis is progressing as planned, and may give hints as to what is happening with the iron. For example the colour of the iron as the reaction progresses. The hydrophobicity of the final gel can also be tested before and after annealing by adding a drop of water to the powder. The finished powders were also rudimentally checked for magnetic properties by moving a neodymium magnet over them.

3.3.1 XRD

XRD was performed on powdered samples, and the apparatus used was a D8 Advance DaVinci X-ray Diffractometer with a CuKα radiation source and a LynxEye™ detector. All samples were run using the same program from 5° to 75° 2θ at 0.1° intervals.

3.3.2 Nitrogen isotherms

Nitrogen isotherms were measured using a Micrometrics Tristar 3000, Surface Area and Porosity Analyzer. Both adsorption and desorption curves where measured to perform BET and BJH analysis. Beforehand the samples were degassed using a Micrometrics VacPrep 061 Sample Degas System to remove water and other volatile adsorbents. Degassing occurred at 250° under vacuum for several hours.

3.3.3 ICP-MS

ICP-MS was performed by first digesting the samples in nitric acid and fluoric acid. Pore water samples were also digested due to the possible presence of silica colloids. The dissolved samples were suitably diluted and analysed with an Element 2™ instrument from Thermo.

3.3.4 UV-vis

UV-vis was performed on the powders using a PerkinElmer Lambda 750 UV-vis spectrometer with a D2 and Tungsten lamp. The spectra analysed ran from 220 nm to 800 nm with a step length of 2 nm.

3.3.5 XAS

XAS was performed at the Swiss-Norwegian beamlines (SNBL) at the ESRF synchrotron, Grenoble, France. The model compounds iron, wustite, magnetite and hematite were also analysed as they were needed for further analysis of the data. Data analysis was done with the software Athena 0.8.056 for XANES and to clean up the data. EXAFS analysis was done with DL Excurv v1.0b.

Pre-edge peak fitting was done in Athena by fitting a arctan function for the edge background and a Gaussian function for the pre-edge peak. The fitting was done in the region from the K-edge to 16 eV below the K-edge. In some cases Athena could not fit a reasonable pre-edge centroid position, and it was fitted manually. This was done by incrementally changing the value to optimize the fit value, but as a result the uncertainty could not be calculated.

EXAFS fitting was done by refining the variables shell by shell, and the Z+1 core hole approximation was used for iron. Fourier filtering was attempted at several intervals in the region of interest until one was found that isolated one peak in the FT curve. The AFAC value was fitted with hematite.

4 Results

4.1 Simple Observations

The waterglass and SA appeared as colourless liquids slightly more viscous than water, depending on the dilution. SA had a pH measured consistently between 2-3, and even a few drops of non-ion exchanged waterglass or a base would induce gelling.

Upon addition of ferric nitrate the waterglass solution quickly gained a clear golden/orange hue as the salt dissolved easily (Fig 4-1). This colour change was always accompanied by a further drop in pH dependent on the amount of ferrous nitrate added. For higher concentrations of Fe^{3+} the pH would easily drop below 1, though this did not seem to induce gelling to any noticeable degree. The intensity of the orange colour also seemed correlated with the ferrous nitrate concentration at this stage, with higher concentrations showing a more intense colour.

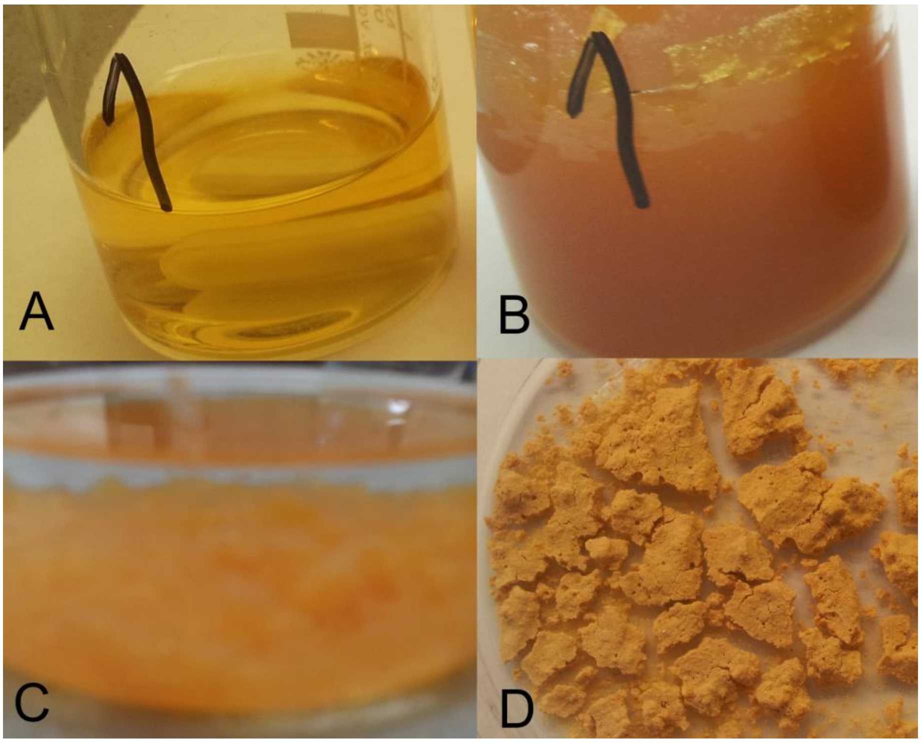

Figure 4-1: The sample FeAG 5 at different stages during synthesis. A: silisic acid solution. B: Hydrogel. C: Surface modification and solvent exchange. D: Dried powder.

Silylation reagents were always added HMDSO first and under vigourous stirring. HMDSO never seemed to give any immediate effects and HMDS was added within seconds. Upon addition of HMDS the golden/orange colour darkened to a more intense orange or sometimes brown (Fig. 4-1). This effect varied wildly, with the high iron containing syntheses like FeAG 10, 11 and 12 turning from clear orange to a dark, opaque brown. On the other hand, for low iron content like FeAG7 the effect was barely noticeable, darkening only slightly to a light yellow. In all cases the colour change occurred as the pH rose and until the gelling process started. There was still a noticeable correlation between colour and original ferrous nitrate content (fig. 4-2).

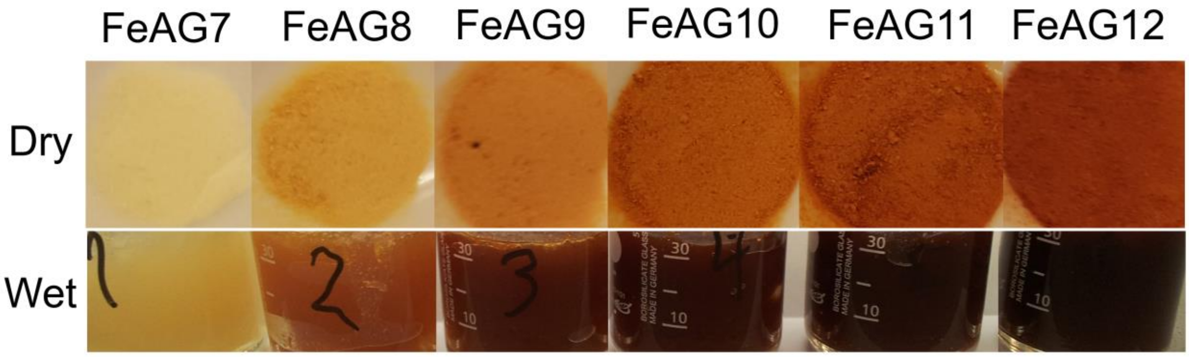

Figure 4-2: FeAG 7-12 from left to right. Above: hydrogel stage. Below: Aerogel stage. Synthesis parameters are similar except increasing iron content from left to right.

The gelling process started quickly upon addition of HMDS. At first the colour change was the only noticeable difference, but soon the solutions started becoming more viscous, opaque and grainy. At one point the solution becomes so viscous that the magnetic stir bar can no longer move it. This happens suddenly, and is considered the point where gel time and gelling pH is measured. The gelling pH was mostly found to be between 7 and 8, with some outliers closer to 9. The gelling time varied from almost immediate to a minute. The gel time was difficult to measure accurately, as the gelling point is slightly subjective, but addition of more ferrous nitrate generally sped up the process. This was especially evident when comparing with plain silica aerogels. The plain gels took considerably longer to gel, often several minutes and at higher pH. Porewater samples extracted from the gels later showed a final pH of 10-11.

After covering the resulting gels with heptane they were all allowed to surface modify for roughly 24 hours. The amount of pore water expelled by the hydrophobic gels varied, but are hard to quantify. The colour grew only slightly lighter throughout the surface modification and solvent exchange (Fig.4-1). The pore water was completely clear.

After evaporating away the heptane solvent the colour changed again for a lighter hue (Fig 4-1 and 4-2). This effect was most noticeable for the gels with high ferrous nitrate concentrations. In these cases the finished dry gels returned to a lighter orange or brown more reminiscent of the original Fe^{3+} waterglass solution, but still a bit darker. This was a general trend for all colour changes discussed so far: Syntheses involving more iron had more apparent change, while low iron content was at times barely noticeable as seen in figure 4-2.

Mortaring the finished gels and adding a drop of water to the samples showed that the finished product was indeed hydrophobic. This property disappeared as the gels were annealed. Water would now wet the material, and the flow properties of the powder improved. The annealing process also caused a final colour change. Once again the samples grew darker, this time almost uniformly for all samples regardless of iron content. The final colour was also a bit muted sometimes a faint grey tinge could be seen.

Using a neodymium magnet and moving it across the outside of the sample glass container no immediate magnetic properties could be seen.

For some syntheses with high iron concentrations the gelling step was not only fast, but noticeably exothermic. This was particularly noticeable for FeAG12.

4.2 XRD Results

Figure 4-3 shows the XRD diffractograms of several samples. The diffractograms show a varying degree of crystallinity from completely amorphous to the emergence of up to five diffraction peaks. The peaks appear at $2\theta = 29°$, 33°, 17°, 22° and a double peak at 40°. Although not all samples show all peaks, their position are the same. The most prominent diffraction pattern is seen for FeAG12, but FeAG11 and FeAG10 also show all five peaks, though some are very weak. These three samples are also among those with the highest theoretical iron content based on synthesis parameters, but FeAG6 with a comparable theoretical iron loading to FeAG12 has a notably less prominent pattern. The samples FeAG1 and FeAG5 has no diffraction pattern and has a very low theoretical iron loading, but FeAG5, 7 and 8 have similar loadings and show a small peak emerging at 29 2θ. There is a general trend between the number of diffraction peaks and their strength and the hypothetical iron content, but not a perfect trend, as some samples like FeAG6 and FeAG5 break the pattern.

The peak at 29° 2θ always seem to show up first and is the most prominent. After this the peaks at 33° and 22° show up. The last two peaks at 17° and 40° tend to appear last and are the least prominent when they do.

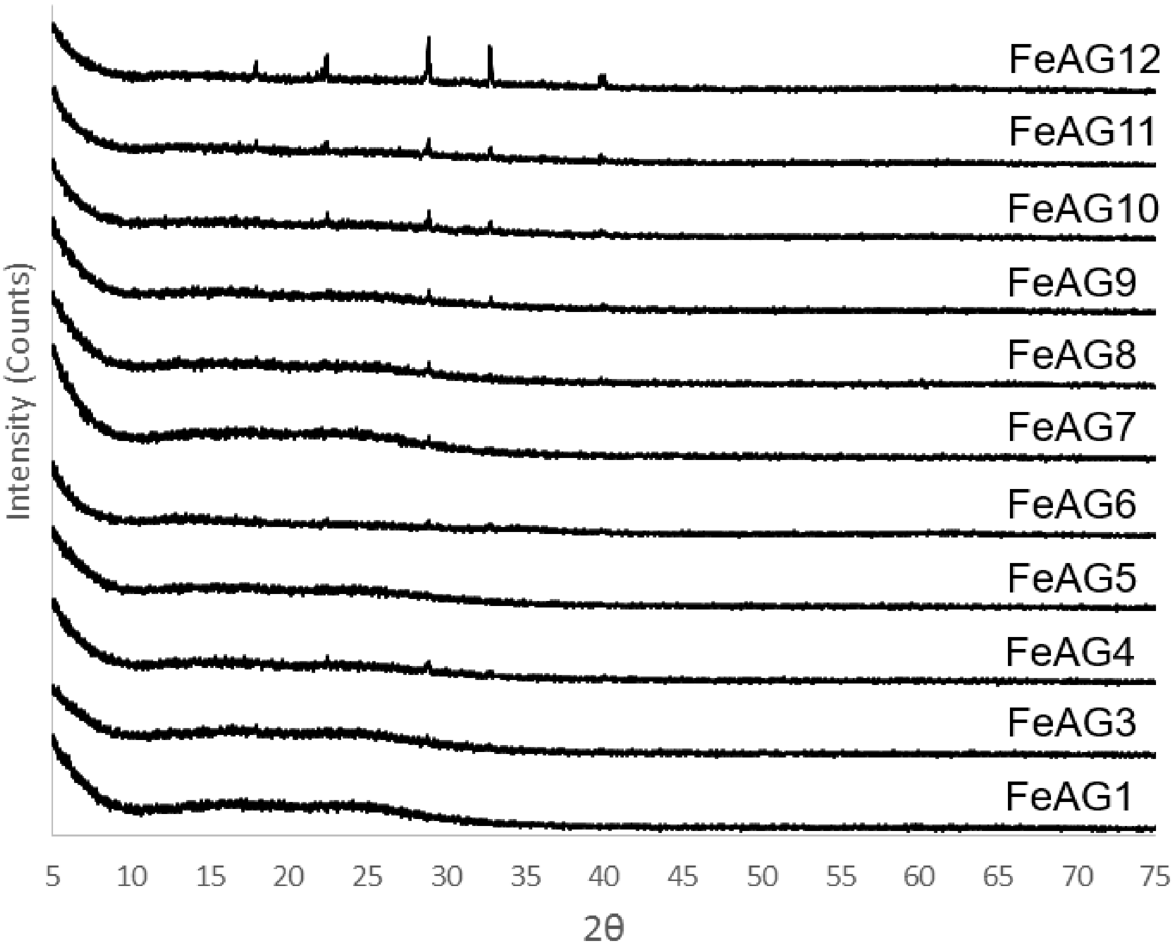

Figure 4-3: All available XRD diffractograms for iron containing aerogel samples taken before annealing.

For comparison with the FeAG samples, the diffractogram for PAG2 is shown in figure 4-4. No clear diffraction pattern or peaks are visible.

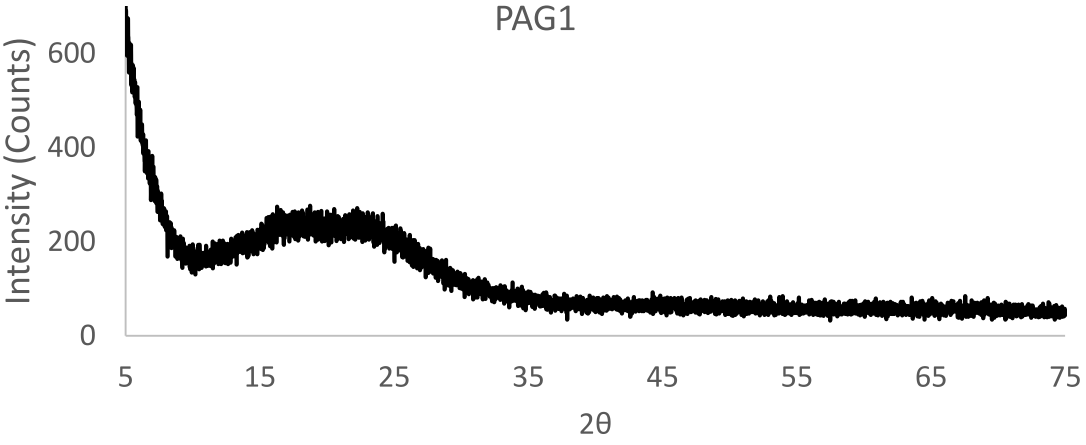

Figure 4-4: Diffractogram for the plain silica aerogel sample PAG2.

Some samples were annealed at 450 °C, and the comparison of XRD diffractograms before and after are shown in figure 4-5. FeAG1 had no diffraction pattern to start with, and annealing did not cause any new peaks to appear. FeAG7 had a small peak at 29° 2θ. After annealing it disappeared completely. FeAG12 had the most severe diffraction pattern of all samples. After annealing no pattern could be seen.

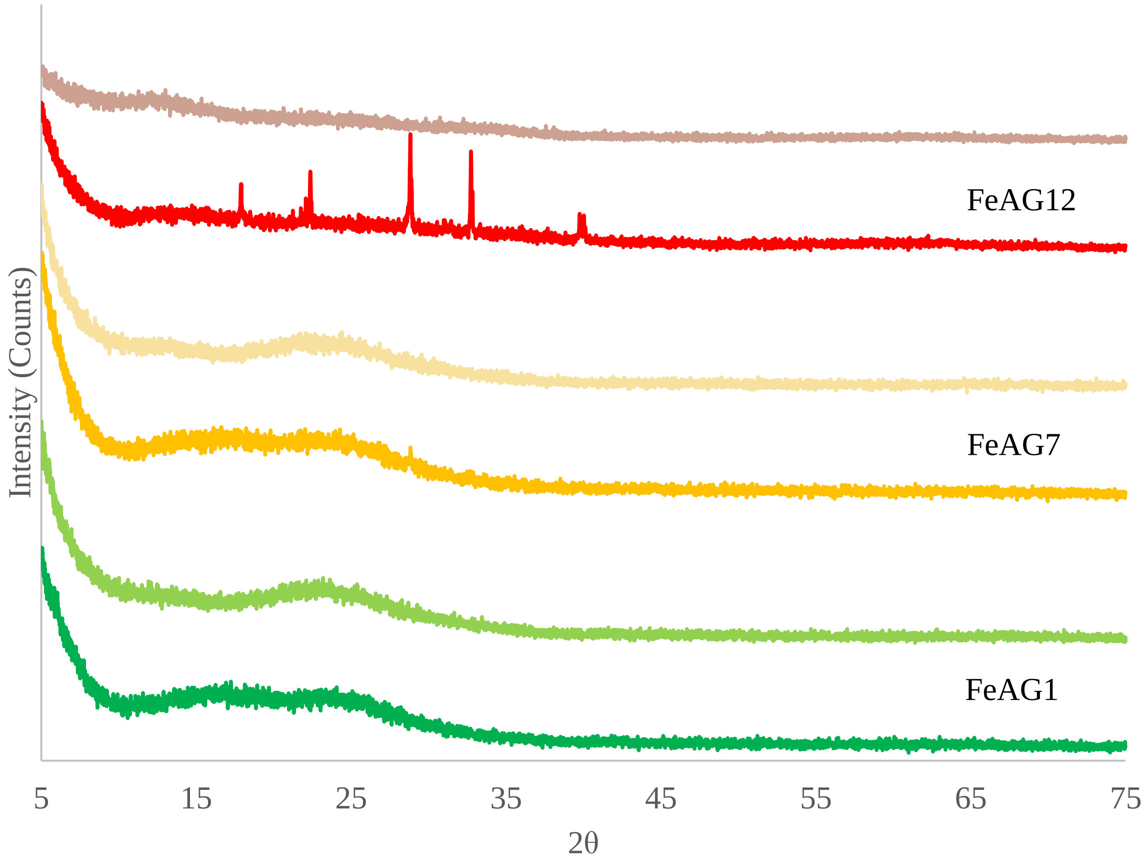

Figure 4-5: XRD diffractograms of samples FeAG1, 7 and 12. Lower plots: Before annealing. Upper plots: After annealing.

4.3 Nitrogen Isotherm Results

The adsorption and nitrogen isotherms for certain samples can be seen in figure 4-6, and the results for surface area, pore volume and average pore diameter in table 4-1. The results show samples with porosities ranging from 52.5% for FeAG9 to 68.0% for FeAG1. The average pore diameters for all samples range from 33.3 Å for FeAG8 to 44.7 Å for FeAG1, all falling within the mesopore range. Surface areas vary from 541.8 m^2/g for FeAG2 to 701.3 m^2/g for FeAG7.

The plain sample with no iron, PAG2, shows a porosity of 63.3%, higher than most samples, but lower than some. The average pore diameter is 35.6 Å which is among the lowest, and the surface area of 754.1 m^2/g is the highest by a fair margin.

Table 4-1: Surface data from isotherms. Specific surface area from BET, Pore diameter and pore volume from BJH and desorption curves and porosity calculated from pore volume.

Sample	**SSA BET (m^2/g)**	**D_p BJH Des. (Å)**	**V_p BJH Des. (cm^3/g)**	**Porosity (%)**
FeAG1	655.5	44.7	0.967	68.0
FeAG2	541.8	43.4	0.665	59.4
FeAG3	698.9	41.0	0.888	66.1
FeAG4	612.9	41.7	0.692	60.3
FeAG7	701.3	38.5	0.871	65.7
FeAG8	622.5	33.3	0.584	56.2
FeAG9	549.4	34.8	0.502	52.5
PAG2	754.1	35.6	0.769	63.3

The isotherms in figure 4-6 all contain a hysteresis loop. All isotherms have the same general shape, with a long and horizontally drawn out flat hysteresis loop. Some samples have a steeper curves than others with FeAG1, 3 and 7 being the steepest. Their hysteresis loops end at roughly 500 cm^3/g and are those with highest porosity as well.

The isotherm for PAG2 is similar to the iron containing ones, but with some differences. The part of the isotherm at low pressure, the BET range relating to surface area, is steeper than any other sample. The hysteresis loop extends below a relative pressure of 0.2 while all others end at 0.4. To complement the average pore diameters in table 4-1, the pore distributions calculated by BJH is shown in figure 4-7.

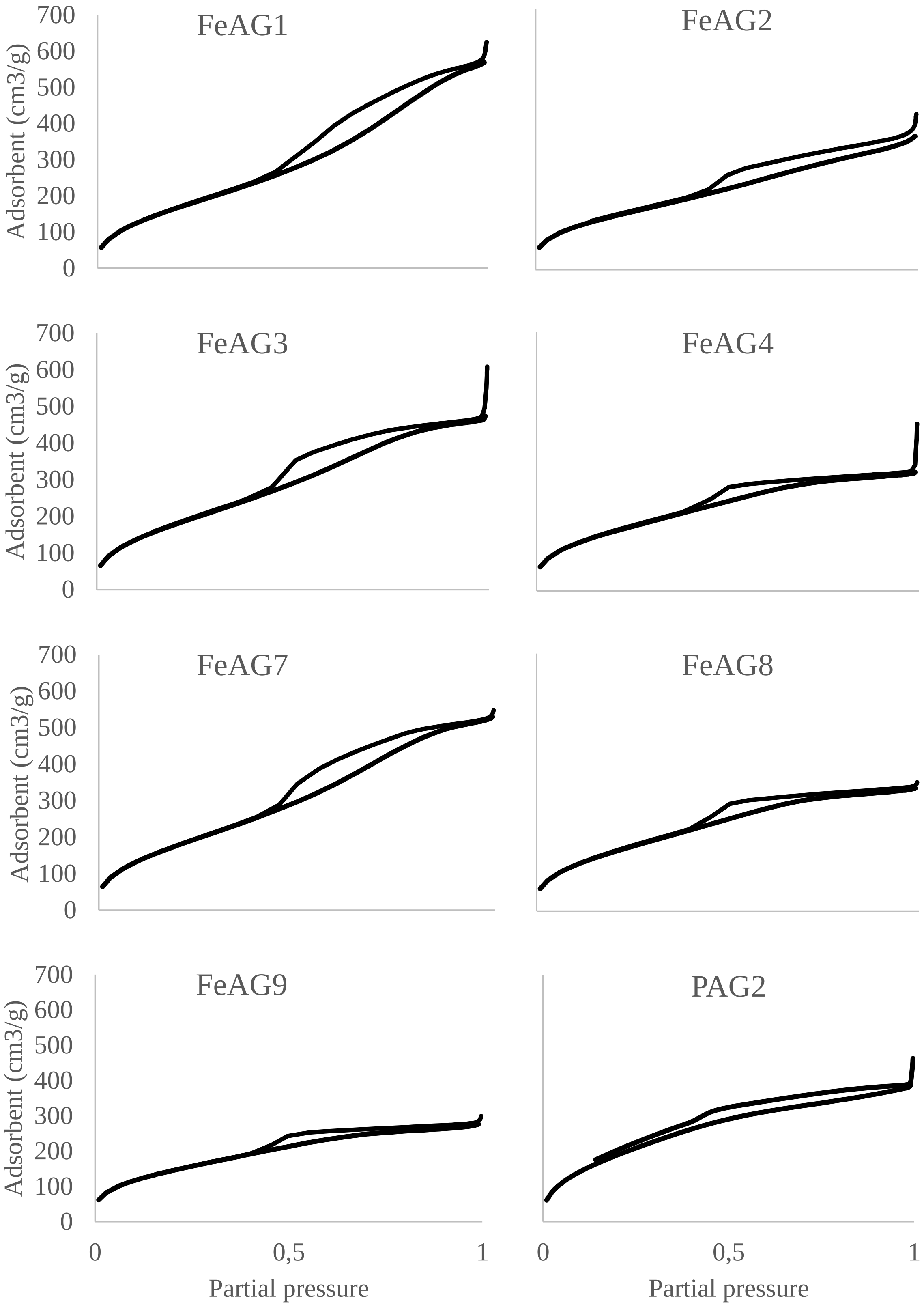

Figure 4-6: Nitrogen isotherms for various samples. Adsorption and desorption curves plotted together to form hysteresis loops.

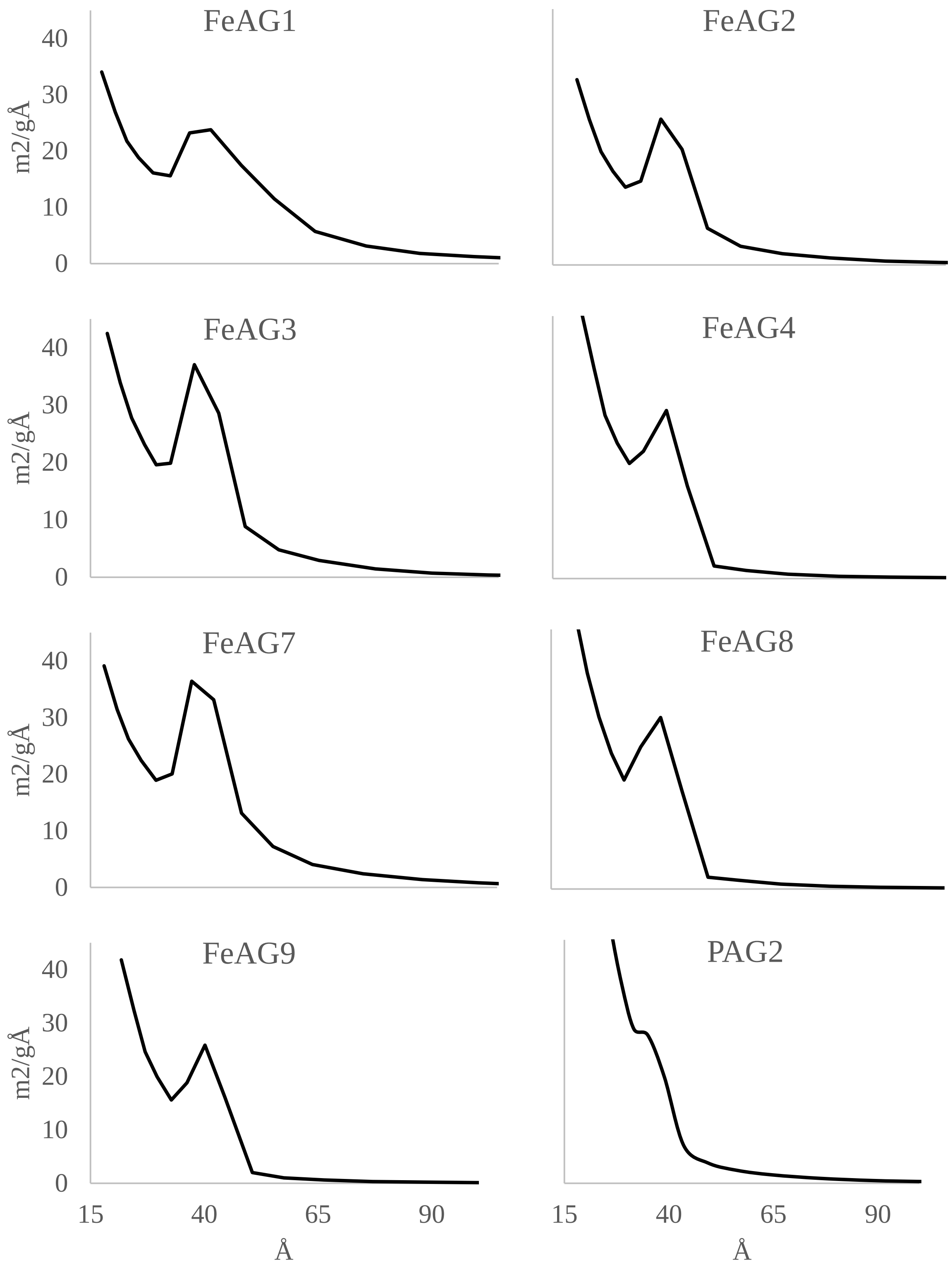

Figure 4-7: The pore distribution of various samples. Plots show a range from 15 Å to 100 Å, though the plots sometimes cut off for the smaller pore sizes due to limitations of the instrument.

The pore distributions for iron containing samples show a clear peak in the mesopore range centred at 35-40 Å. To the left all samples also have a large shoulder rising into the micropore range to the right a tail of varying size extending towards even higher pore diameters. FeAG1 has a particularly wide mesopore peak with a prominent tail ranging far to the right. At the same time the shoulder extending toward the micropore region is more subdued than any other sample. FeAG1 is also the sample with the highest average pore diameter. Samples FeAG4, 8 and 9 have relatively small mesopore populations, but more of the smaller pores.

PAG2 has a very different pore distribution compared to the iron containing gels. Two distinct populations of pore sizes are visible, but the mesopores are centred at a relatively low 35 Å. The shoulder of smaller pores is by far the most prominent appearing steeper than for any of the other. PAG2 contains far more smaller pores than the other samples, lowering the average pore diameter.

4.4 ICP-MS Results

The measured iron content from ISP-MS, as well as the theoretical Fe^{3+} content is shown in table 4-2. ICP-MS was also used on pore water samples from FeAG 7-13. No statistically relevant iron content was found in any of them. FeAG12 and 13 has a similar loading f 10 wt% iron. This is of particular note as FeAG12 has roughly 1.6 the theoretical iron content of FeAG13.

Table 4-2: The measured iron content by ICP-MS of final products and from reagent added to synthesis.

Sample	Fe (wt%) ICP-MS	RSD (%) ICP-MS
FeAG1	4.02	2.1
FeAG3	3.82	2.3
FeAG4	6.71	2.1
FeAG7	3.07	2.2
FeAG8	6.81	0.9
FeAG9	7.82	1.8
FeAG12	10.01	1.0
FeAG13	10.48	0.8

4.5 XAS Results

XAS was performed on four model compounds, iron metal (Fe), wustite (FeO), magnetite (Fe_3O_4) and hematite (Fe_2O_3). The XANES spectra for these model compounds are shown in figure 4-8. XAS was then performed on the samples FeAG1 and FeAG7 both before and after annealing. Figure 4-9 shows the XANES spectrum for these samples.

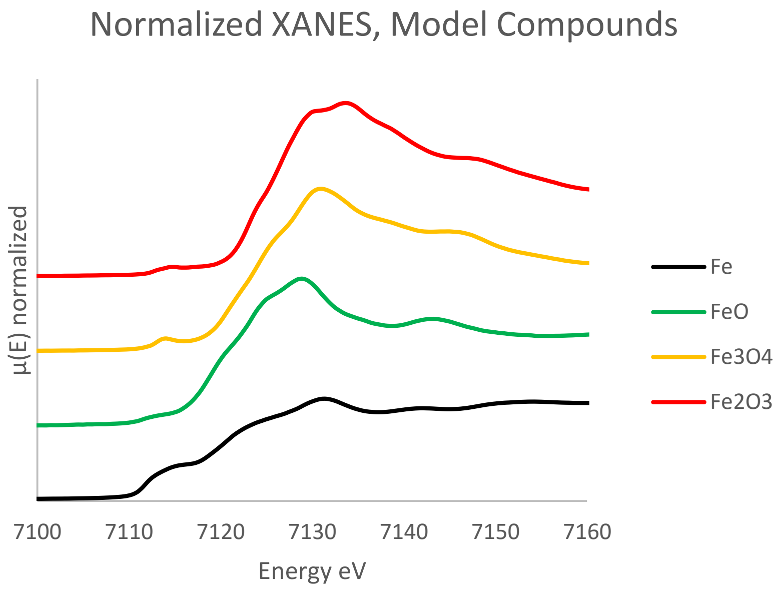

Figure 4-8: Normalized XANES for model compounds. From the bottom: Iron metal in black, wustite in green, Magnetite in yellow and hematite in red.

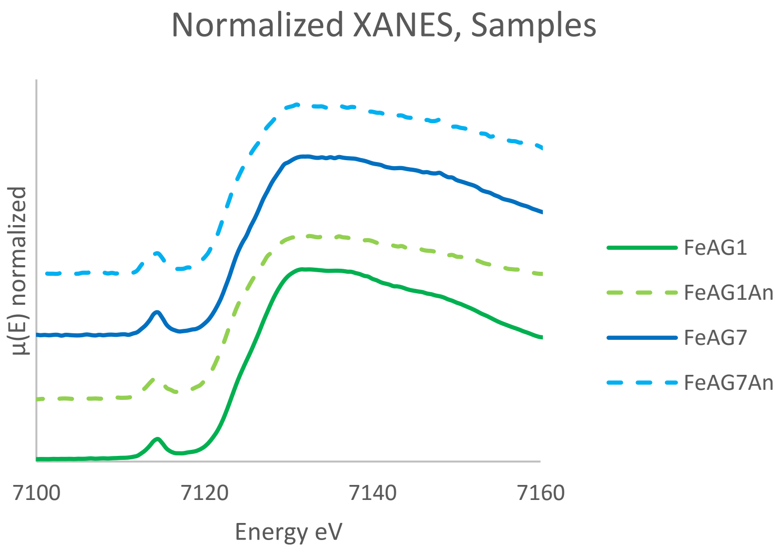

Figure 4-9: Normalized XANES for samples. On the bottom in green: FeAG1. On the top in blue: FeAG7. Dotted lines are samples after annealing.

The measurements of the K-edge and pre-edge position as well as the pre-edge intensities are shown in table 4-3. The position of the K-edge does not vary for the samples except for moving 1 eV lower after annealing. In both cases the value of E_0 is very close to hematite at 7123.9 eV.

The pre-edge is also largely unchanged at roughly 7114 eV even after annealing, though the uncertainty of these values is considerable, and the values for FeAG7 and FeaG7An had to be manually fitted. The same had to be done for wustite.

The pre-edge intensity is at roughly 0.25, though FeAG7An drops considerably to 0.20. A pre-edge at 7114 eV is similar to hematite and magnetite relative to wustite, and the intensities of 0.2 and above are the largest values measured among samlples or known model compounds.

Table 4-3: Values for the K-edge position and pre-edge peak fitting for FeAG1 and 7 before and after annealing as well as the four model compounds.

Sample	**K-edge (E_0/eV9**	**Pre-edge (eV)**	**Pre-edge intensity**	**Pre edge fit value (R/%)**
FeAG1	7124.5	7114.1(1.5)	0.24(6)	0.0037
FeAG1An	7123.5	7114.0(2.1)	0.26(8)	0.0044
FeAG7	7124.5	7114.3(-)	0.27(4)	0.0059
FeAG7An	7123.5	7114.1(-)	0.20(6)	0.015
Fe	7112.0	-	-	-
FeO	7120.3	7113.6(-)	0.11(7)	0.0038
Fe_3O_4	7122.5	7114.5(3.8)	0.2(1)	0.0039
Fe_2O_3	7123.9	7114.4(3.3)	0.19(9)	0.0038

For EXAFS the AFAC value was refined using hematite and was found to be 0.7445. Magnetite was also fitted for use in later comparisons. The EXAFS fitting values for hematite and magnetite is seen in table 4-4.

Table 4-4: EXAFS fitting data for Hematite. Multiplicities N are given from theory [55], and allows us to calculate AFAC to be 0.7445. Number in parenthesis denote the uncertainty of the last given digit.

Sample	**Shell**	**N**	**R (Å)**	**$2\sigma^2$ (Å 2)**	**R (%)**	**Δk**
Hematite	Fe-O	3	1.984(8)	0.015(3)	36.34	2.5-15
Fe_2O_3	Fe-O	3	2.18(2)	0.03(1)		
	Fe···Fe	1	2.896(8)	0.005(2)		
	Fe···Fe	3	3.008(5)	0.009(1)		
	Fe···Fe	3	3.40(1)	0.016(3)		
	Fe···Fe	6	3.713(7)	0.017(2)		
	Fe···Fe	1	3.92(2)	0.008(4)		
Magnetite	Fe-O	1.33	1.92(3)	0.02(1)	39.35	2-26
Fe_3O_4	Fe-O	4	2.06(1)	0.019(4)		
	Fe···Fe	4	3.010(8)	0.017(2)		
	Fe···Fe	8	3.410(7)	0.014(2)		
	Fe···Fe	4	3.67(2)	0.018(5)		

Using hematite and the fitted values above an AFAC value was approximated to 0.7445. The rest of the samples were now fitted, starting with the samples FeAG1 and FeAG7 before annealing. The plots and resulting FT curves can be seen in figure 4-10.

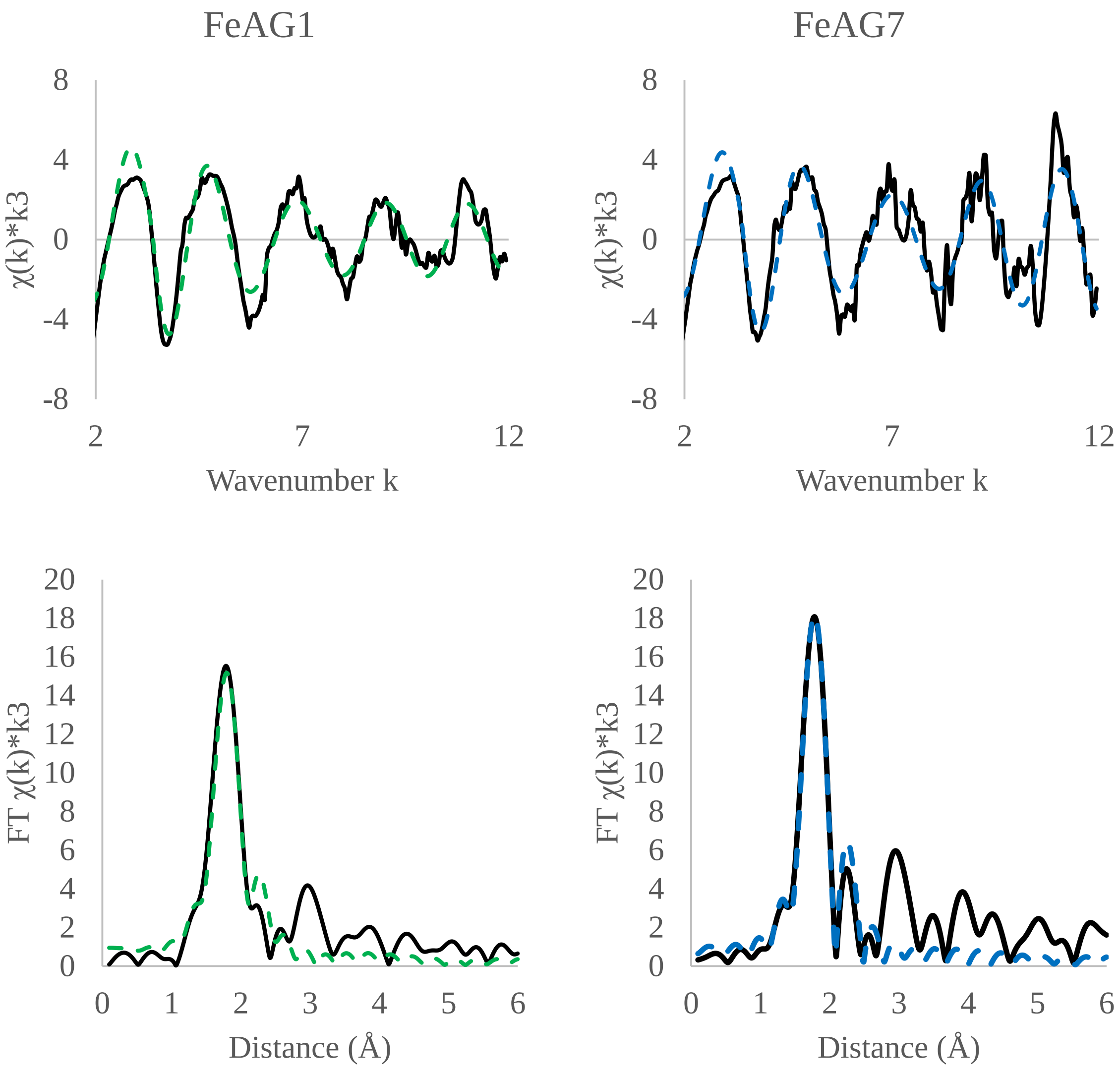

Figure 4-10: Chi curves and FT curves for samples FeAG1 (left) and FeAG7 (right) with experimental data in solid black and fitted lines in dotted green or blue.

The next shells, located at approximately 3 Å could not be fitted normally, and fourier filtration was used to find the shells in this region. The filtration for both samples was between 2.6 and 3.0 Å and three different fits were attempted. First a solitary Si shell, then a solitary Fe shell and lastly a combination of the two. The R values were then used as an indication for which case was most likely.

The fitting for the fourier filtering of FeAG1 can be seen in figure 4-11 and the same plot for FeAG7 in figure 4-12.

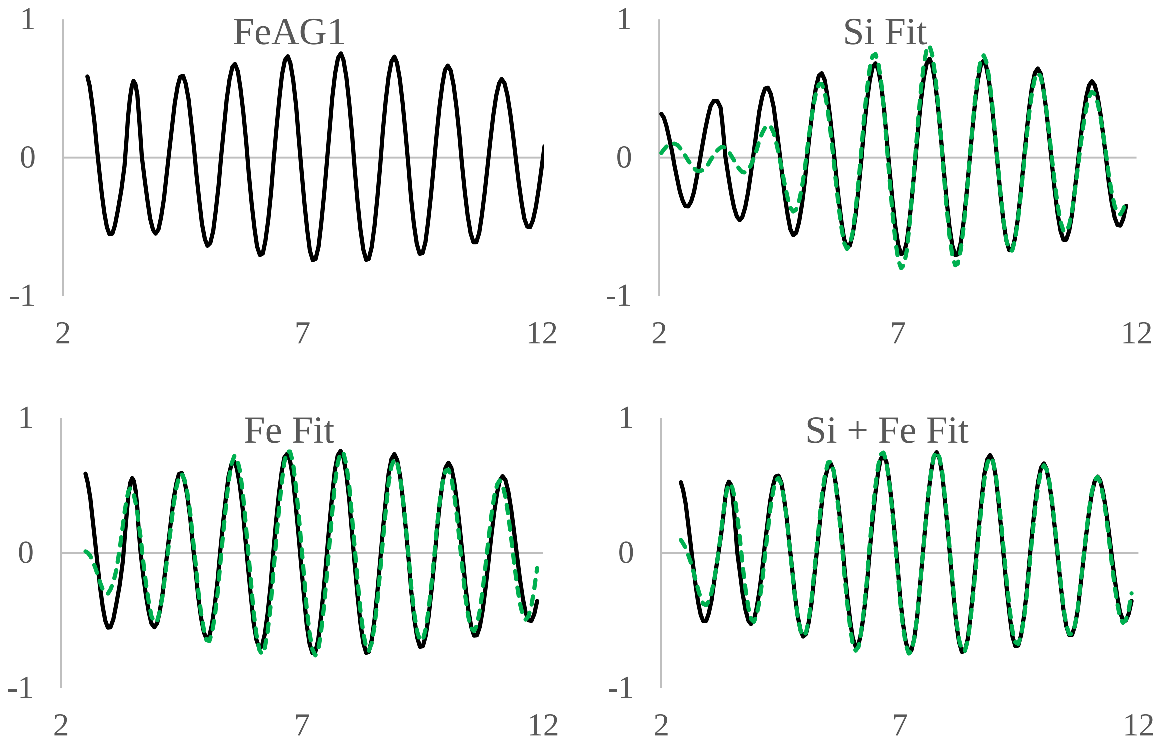

Figure 4-11: EXAFS fit for FeAG1 using fourier filtration at 2.6 to 3.0 Å. Curves show attempts at fitting Fe and Si shells both alone and together.

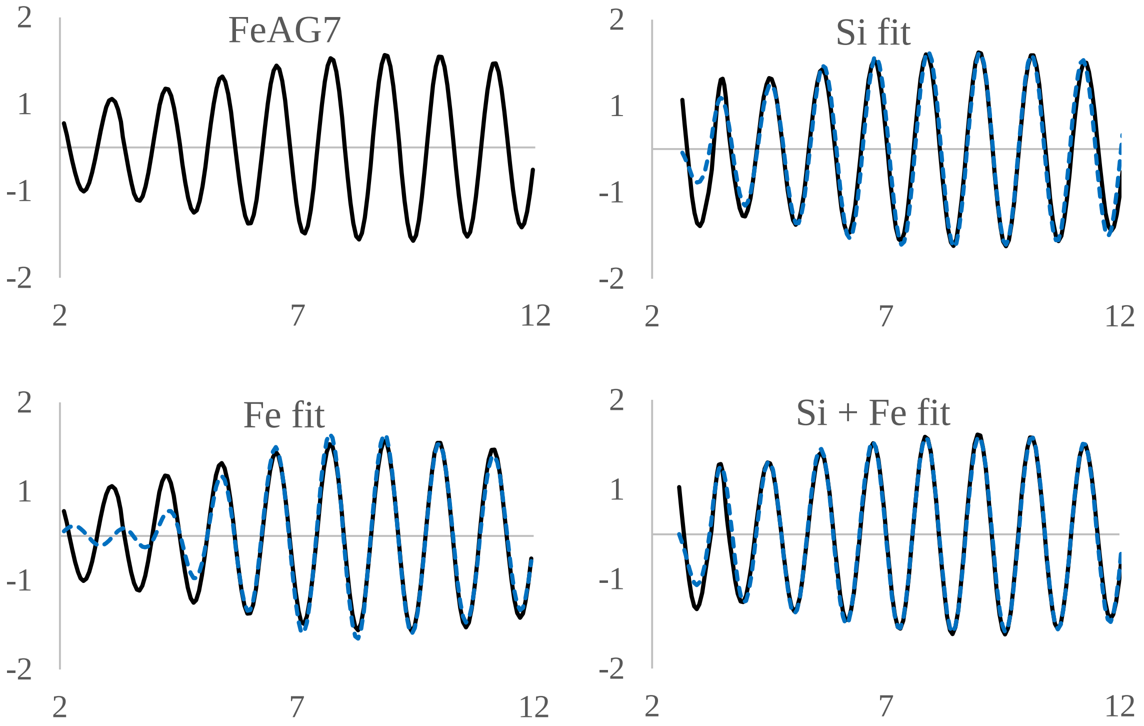

Figure 4-12: EXAFS fit for FeAG7 using fourier filtration at 2.6 to 3.0 Å. Curves show attempts at fitting Fe and Si shells both alone and together.

The resulting R-values are shown in table 4-4, and the EXAFS fitting parameters, assuming both a Si and Fe shell, are shown in table 4-5. The R-values show that the combination of both an iron and silicon shell is the most likely scenario, the values being less than half that of any other solitary shell.

Table 4-5: R-values for EXAFS fitting using fourier filtration.

Sample	Si (R/%)	Fe (R/%)	Si+Fe (R/%)
FeAG1	26.08	23.82	10.80
FeAG7	20.17	23.61	8.665

Table 4-6: EXAFS fitting parameters for samples FeAG1 and 7, first for two oxygen shells, then for fourier filtration at 2.6-3.0 Å. AFAC value at 0.7445. Numbers in parenthesis denote the uncertainty at the last given digit.

Sample	Shell	N	R (Å)	$2\sigma^2$ (Å 2)	R (%)	Δk
FeAG1	Fe-O	1.7(3)	1.882(6)	0.002(2)	37.11	2-12
	Fe-O	3.4(6)	2.06(2)	0.033(9)		
FeAG7	Fe-O	2.6(2)	1.878(5)	0.001(1)	41.92	2-12
	Fe-O	1.7(3)	2.10(1)	0.006(3)		
Fourier filtration, 2.6-3.0 Å						
FeAG1	Fe···Fe	0.8(1)	3.066(2)	0.021(2)	10.80	2-12
	Fe···Si	1.20(6)	3.143(2)	0.0064(8)		
FeAG7	Fe···Fe	0.9(2)	3.06(1)	0.018(5)	8.665	2-12
	Fe···Si	1.6(1)	3.125(7)	0.0036(7)		

EXAFS fitting for the annealed samples was more difficult than for the fresh samples due to noisier data. The same process as above was attempted, but with mixed results. Both samples FeAG1An and FeAG7An were fitted with two oxygen shells and refined shell by shell, but the fitted Debye-Waller factors converged to negative values.

When attempting a fourier filtration at 2.7-3-3 Å another problem arose for FeAG1An. The solitary Fe and Si shells both fit remarkably well with similar R-values below 20, but when attempting to fit both shells the Fe···Fe shell gave only a negative Debye-Waller factor. The R-value was larger than for any of the single shell fits, unless the Fe···Fe shell multiplicity was allowed to converge to zero. In this case the R-value was similar to that of a single fitted Fe···Si shell. Trying to fit the Fe···Fe and Fe···Si shells without fourier filtration caused the opposite problem, the Fe···Si shell refusing to fit. Thus we can say nothing conclusive about FeAG1An. Unfortunately similar problems arose for the fitting for FeAG7An, and no EXAFS data can be presented for the annealed samples.

4.6 UV-vis Results

The results for the UV-vis spectroscopy for all samples containing iron is shown in figure 4-13, and for PAG2 in figure 4-14. All samples show the same CT-feature at low wavelengths with two peaks at ca. 230 nm and at 280-290 nm, though finding their exact position is hard as the CT-feature is diffuse. All samples also show absorptions at larger wavelengths in the form of a tail feature. This tail is less prominent for samples like FeAG3 and 7 with low theoretical iron content, and more prominent for FeAG4 and 9 with higher contents. A final feature is seen at 450-460 nm on all samples. After annealing the main features stay the same, but are muddled by the tail feature growing more intense.

The plain aerogel show very little absorption across the spectrum, except for a small peak at 230 nm and a smaller one at 270 nm. Both are very close to the two peaks seen in the iron containing gels. Annealing removes these peaks.

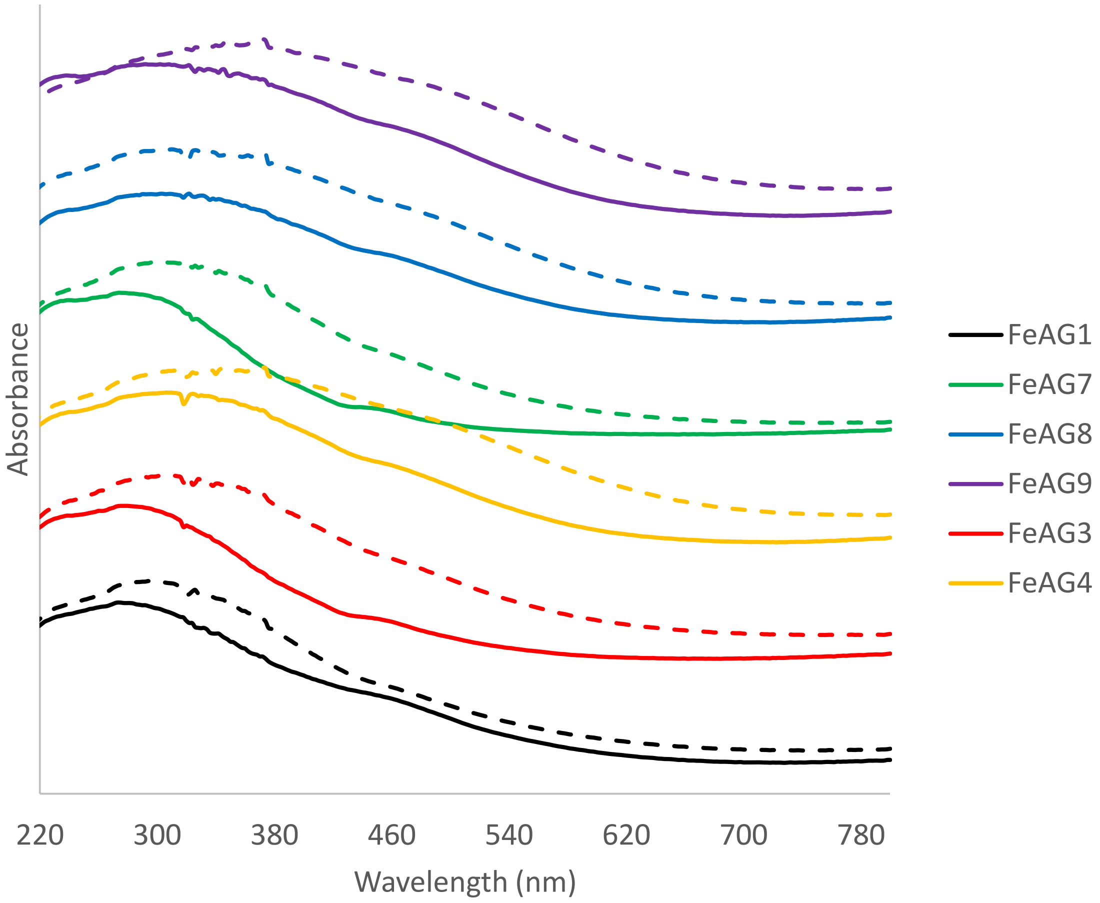

Figure 4-13: UV-vis spectrum for samples FeAG1, 3, 4, 7, 8 and 9 from bottom to top. Dotted lines represents samples after annealing.

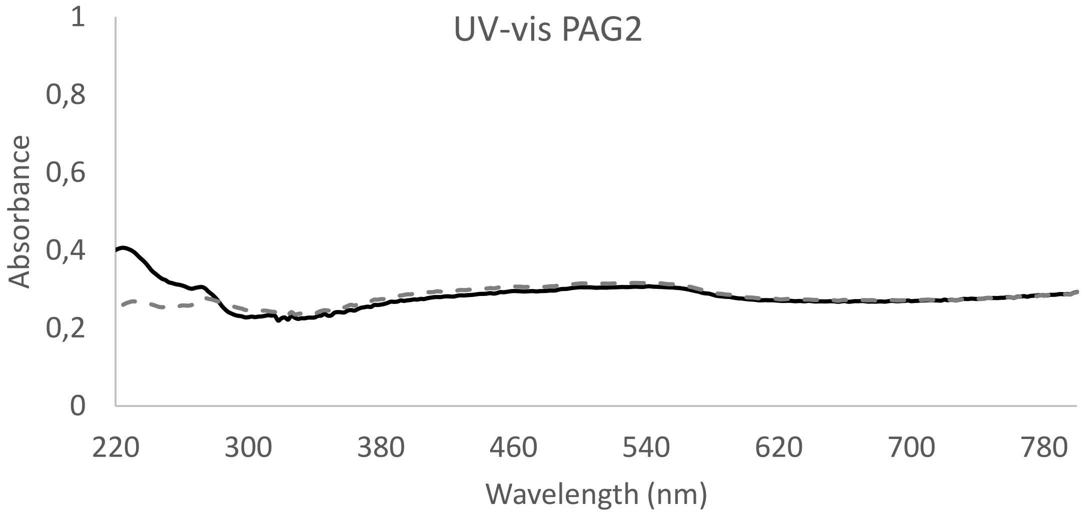

Figure 4-14:UV-vis spectrum for PAG2 a plain silica aerogel. Solid: before annealing. Dotted: After annealing.

From the BET/BJH results regarding porosity and pore distribution it is clear that the synthesized material are indeed aerogels, as they all have high porosities >50% and a hierarchical pore distribution [4]. The ICP-MS results also confirm that iron is present in the samples with loading varying from 3 w% to 10 w%. Using the rest of the results we must attempt to determine the exact species of iron present. We will also look at the effect of the synthesis parameters, especially iron content, of the final product.

XANES and EXAFS are powerful techniques, and we will depend a lot on these results. Since only FeAG1 and FeAG7 were anlalysed by XAS we will be talking about them a lot, and for simplicity we will refer to them by alternate names when appropriate. Based on the iron content found by ICP-MS we rename FeAG1 to FeAG4.02 and FeAG7 to FeAG3.07.

In contrast to the XAS results the UV-vis results are not weighted very heavily. The resulting spectra are difficult to analyse in much detail and much of the underlying theory of the iron spectrum is uncertain.

5.1 The Effect of synthesis parameters

The samples synthesized over the course of this thesis represents some variation in all synthesis parameters. The variable that was most focused on was the iron content, and the data show a clear effect on the final product. Certain effects of other synthesis parameters can also be extrapolated.

5.1.1 Iron content

The best demonstration for the effect of the iron content is batch 5 containing samples FeAG7-12. Since they were all made from the same SA solution divided into six we can completely eliminate interference from variance in the SA and H_2O content. The amounts of HMDSO and HMDZ was also controlled.

The first apparent trend is quite visible in figure 4-12 showing the darkening in colour with iron content. FeAG7 is light yellow, and adding iron darkens the colour to orange and eventually a dark orange-brown for FeAG12. The same samples show increasing degrees of crystallinity from XRD. The conclusion is that adding more iron causes larger crystalline species in the gels which causes the darker colour.

Not all samples were analysed by ICP-MS, but of those that were there is a general trend between theoretical iron content and measure loading shown in figure 5-1. The trend is not perfectly linear shown by FeAG12 and FeAG13. Both have a loading of roughly 10 wt% iron, but theoretically FeAG12 should have 1.6 times the loading of FeAG13.

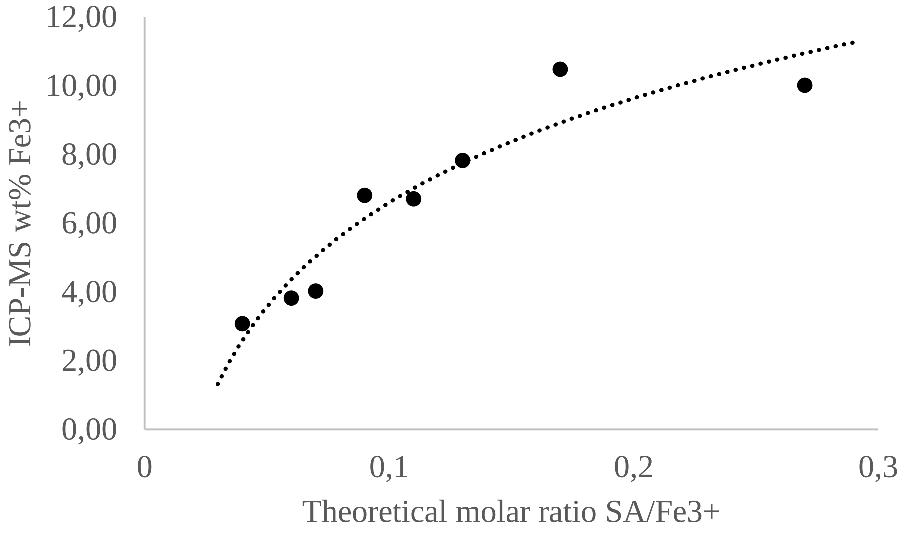

Figure 4-15: The theoretical iron content as a ratio of silisic acid plotted against experimantal values from ICP-MS. The dotted line shows a logarithmic fit with R=0.9.

This trend could be explained by an upper limit for iron loading in silica aerogels, but this is unsatisfactory. The pore water for both FeAG12 and 13 show no iron content whatsoever, and the same is true for all pore water samples tested. All the iron added during synthesis stays in the gel, so the explanation lies elsewhere. The only explanation is that adding iron makes the gel more massive, though it is uncertain how this happens.

Adding iron also has an effect on porosity and surface data. Figure 5-2 compares the data from ICP-MS and BET/BJH and shows a clear trend. Higher iron loadings decrease the specific surface area and pore volume (porosity).

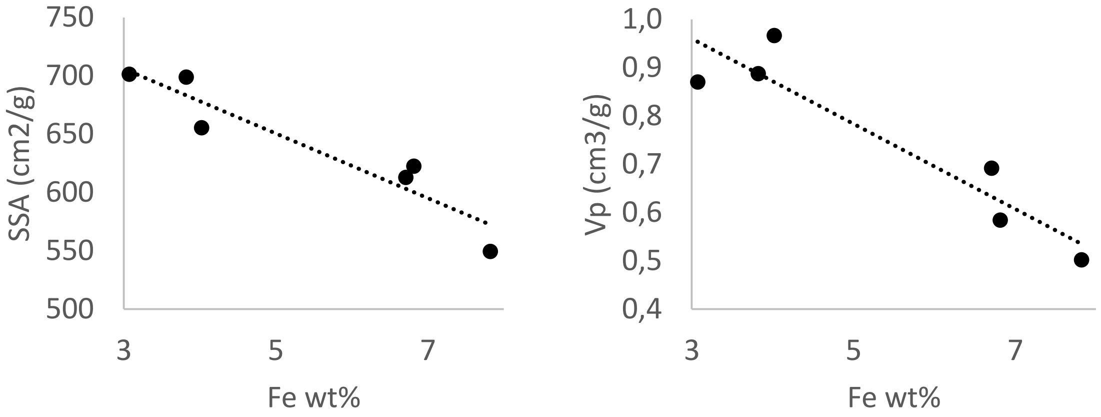

Figure 4-16: The Specific Surface Area (SSA) measured by BET, and the pore volume measured by BJH (Desorption) as a function of iron loading measured by ICP-MS.

Compared to plain aerogels the pore distribution also changed significantly upon adding any iron. PAG2 had a much higher fraction of smaller pores, and the large pores were centred at a lower pore diameter. Adding small amounts of iron increased the average pore diameter. Larger pores have less surface area for more volume so this leads to an increase in porosity and decrease in surface area. Some of the same effects were seen when incorporating copper [5].

5.1.2 Other parameters

Other parameters are harder to study as no proper parameter study was done. The only visible effect of any other parameter is the SA concentrations effect on crystallinity. Though crystallinity increases with iron content within each batch different levels of crystallinity are observed for gels with similar iron content across batches. The SA content is most likely a good contributor to this as HMDSO and HMDS was more easily controlled across batches. Unfortunately SA is the hardest parameter to control due to the ion exchange step in the synthesis, and this must be solved before a good parameter study is performed.

HMDSO and HMDS may also affect the synthesis in unknown ways, particularly in terms of site geometry after annealing. HMDS is especially interesting due to its effect on pH. Unfortunately we can’t say much, as the EXAFS data for annealed samples could not be fitted.

5.2 The Effect of Annealing

So far we have mostly discussed non-annealed samples. Annealing occurred at 450 °C, far higher temperatures than the ones used for the APD step. This leads to the removal of the hydrophobic surface modification, making the gels hydrophilic again. Beyond the removal of the surface modification other interesting changes occur as well.

The most dramatic change is in the crystallinity. The expected results for heating up a iron (III) oxide-hydroxide compound would be a crystalline oxide, probably hematite. The actual results are quite the opposite. From figure 4-5 we see that XRD diffraction of samples FeAG4.02, which showed no diffraction pattern, stayed the same after annealing. No crystalline species appeared. FeAG3.07 had a weak diffraction peak at 29° 2θ, and it completely disappeared. FeAG12, the sample with the most intense diffraction pattern of them all and over 10 w% iron loading also lost all crystallinity after annealing. It seems heat treatment does not promote crystallinity in the samples, but rather removes it. This can be explained in two ways: Either the particles turn amorphous, which seems very unlikely, or they shrink.

One explanation would be interaction with the silica surface. As the surface modifying agents are burnt off the iron is now free to interact with surface silanol groups. Lopez et Al. claims that Fe^{3+} forms octahedral complexes, the silica forming monodentate or bidentate ligands [31]. This interaction is backed up by Pokrovski et Al. who predicts the formation of small octahedral clusters sharing corners with silica tetrahedra [25]. These small clusters are believed to contribute to the tail feature at 300-450 nm in the UV-vis spectrum [26], and this feature is more prominent in samples containing more iron as well as increasing after annealing.

The pre-edge for FeAG3.07 and FeAG3.07An shows a peculiar drop in intensity as well as the appearance of octahedral field splitting upon annealing. Incorporated iron in the silica matrix would probably not be affected, though this could imply that partially tetrahedral nanoparticles shift to octahedral sites. Unfortunately the same effect is not seen in FeAG4.02 and we cannot explain why at this time.

There is not a lot more to say on annealing as the EXAFS data was too noisy to create good fitted functions. The UV-vis data is difficult to interpret, and we hesitate to trust it on more than on basic trends. The effect of annealing is still very interesting, and it is certainly something worth looking into in more detail.

5.3 Determining the iron species

XAS is the most powerful method used, and the XANES results from table 4-3 help us determine some general information about the iron species. Figure 5-3 shows a plot of K-edge position by oxidation state, using the four model compounds to determine the general trend. The K-edge position gives a clear indication of Fe^{3+} in the samples, especially for the non-annealed samples. The pre-edge position can also be used to determine oxidation state. Figure 5-4 shows the pre-edges for the same samples. As we can see from table 4-3 the pre-edges do not change their position when the sample is annealed. The position for all pre-edges are close to 7114 eV.

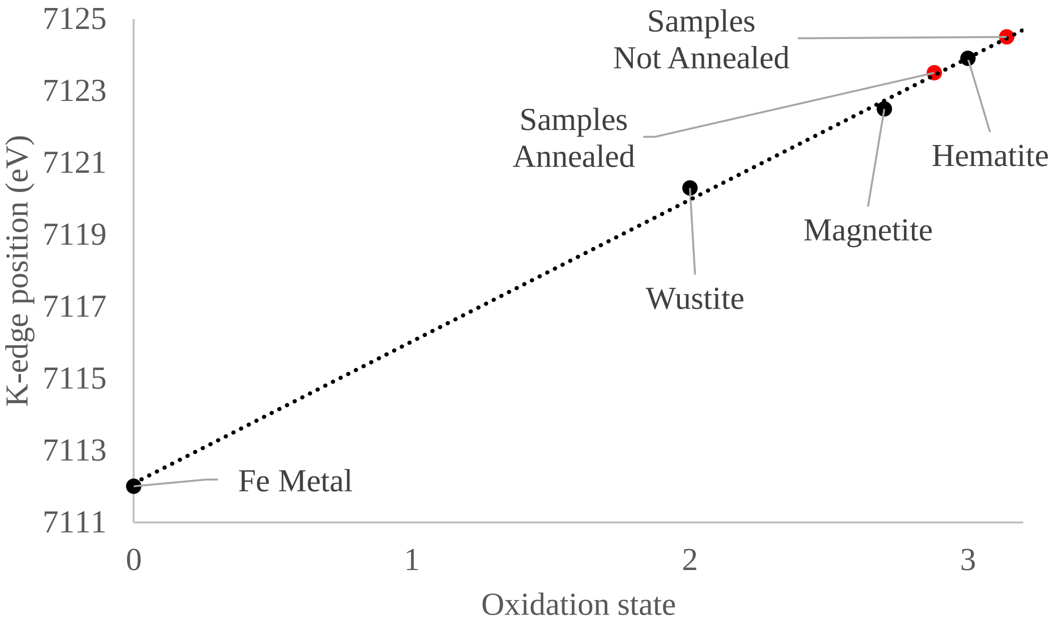

Figure 4-17: XANES K-edge position by oxidation state. Dotted line shows trend predicted by model compounds. Red dots show the predicted positions of samples FeAG1 and 7 before and after annealing.

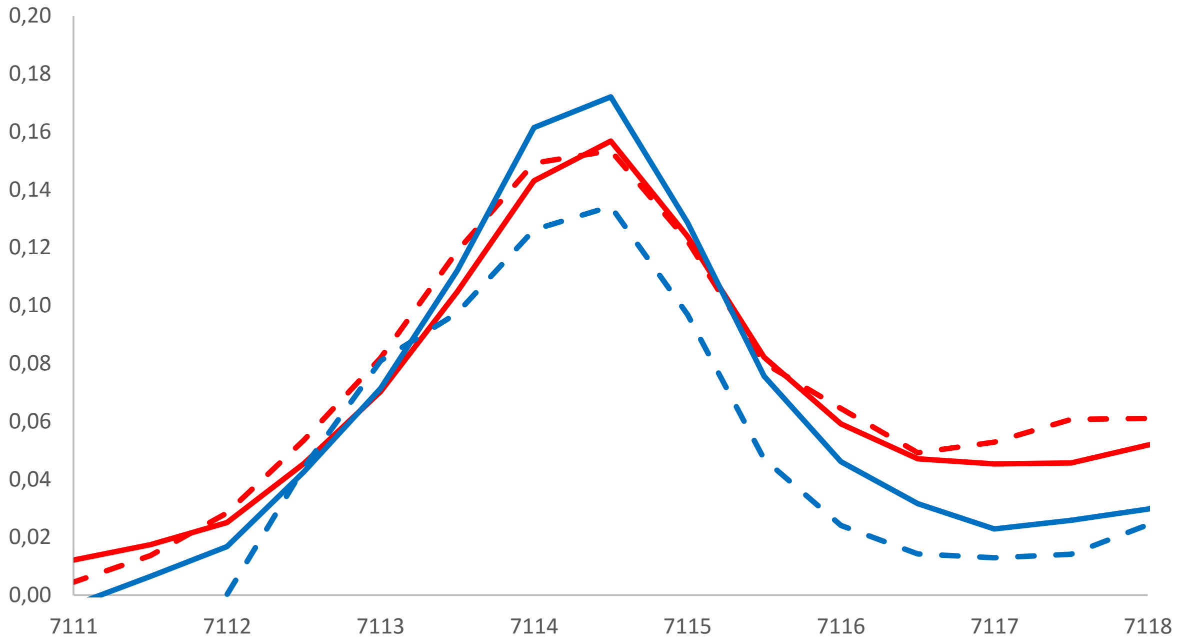

Figure 4-18: The K pre-edges for the samples. Red: FeAG4.02, blue: FeAG3.07 and dotted lines for the annealed samples.

It has been reported that the position of the Fe-K pre-edge changes by a considerable amount given the oxidations state. Wilke et Al. reports 7112.1 eV for Fe^{2+} and 7113.5 eV for Fe^{3+} with mixed oxidation state compound falling between these values [18], though they measured their Fe K-edge at 7111.08 eV, 0.92 eV below ours. Galoisy et Al. reports a wider gap, with Fe^{2+} at 7112 eV and Fe^{3+} at 7114 eV [52]. In either case the position of FeAG1 and FeAG7s pre-edges are a strong indication of Fe^{3+}, especially if the shift in Wilkes data is corrected.

The XANES spectra also gives us rudimentary insight into coordination, mostly through the pre-edge. The measured pre-edge intensities show FeAG4.02 at 0.24 and FeAG3.07 at 0.27. These values are concordant with 4-coordinate systems according to Wilke et Al. [18].

Wilke et Al. performed a thorough analysis on the effects of coordination and oxidation on the iron K-pre-edge [18]. Some of the values from this study was plotted in figure 5-5, as well as the values from our model compounds and samples after correcting for the 0.92 eV shift. The results show that our samples fall within the tetrahedral Fe^{3+} region.

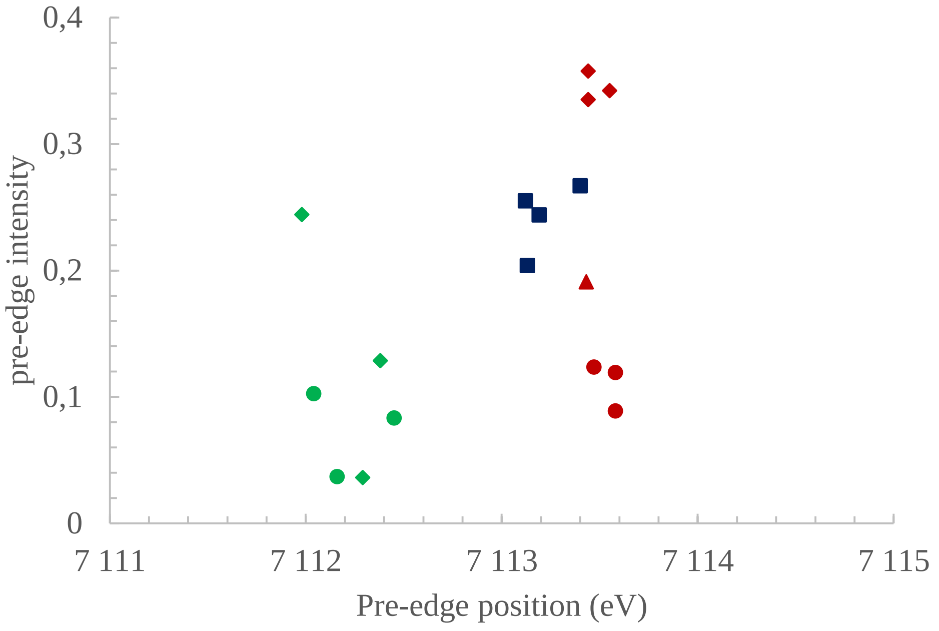

Figure 4-19: Pre-edge data. Green dots represent Fe2+ compounds and red dots represent Fe3+ compounds. Circles are octahedral coordination, diamonds are tetrahedral and triangles or 5-coordinated. Blue squares are samples before and after annealing.

As the precursor used was iron(III) nitrate it is not unexpected that the final product would also be a form of Fe^{3+}. Indeed, the synthesis features no strong reducing agents to facilitate the reduction to Fe^{2+} [30]. Some hypothesize that annealing the samples would cause a reducing environment due to the burning of the hydrophobic surface groups [29], however the K-edge and pre-edge are both indicating Fe^{3+}, so this is most likely not the case.

The pre-edge shape seems to agree with tetrahedral coordination. All pre-edges, except FeAG7An appear as a single absorption peak. This is indicates tetrahedral Fe^{3+} as the Δt splitting energy is very small and may not be resolved [19, 52]. FeAG7An, on the other hand, has the lowest intensity indicating a larger fraction of octahedral Fe^{3+}. For this particular pre-edge we also see a clear shoulder feature at roughly 7113 eV. This shoulder feature is not shifted far enough to imply a fraction of Fe^{2+}, but seem instead to characteristic of Δo splitting from octahedral coordination [52].

The XANES K-edge is difficult to analyse in terms of coordination, though the flat edge crest may indicate low symmetry for the iron sites [51]. This is not unexpected as the silica is amorphous and would not provide a symmetric environment.

More information concerning coordination can be gleamed from the EXAFS results by studying the distance to the first oxygen shells. If the Fe^{3+} sites are tetrahedrally coordinated we expect to see a shorter Fe-O distance than for octahedral coordination. The positions and multiplicity of the first two oxygen shells for FeAG4.02 and FeAG3.07 are seen in figure 5-6, and also the oxygen shells for magnetite (Fe_3O_4) and hematite (Fe_2O_3).

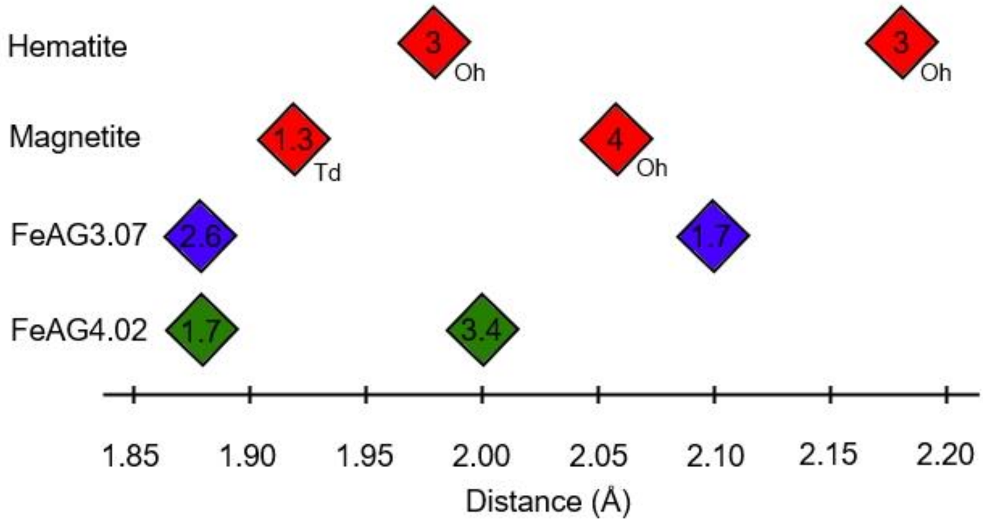

Figure 4-20: The two fitted oxygen shells for hematite, magnetite and the two samples FeAG4.02 and FeAG3.07. Numbers indicate multiplicity.

We can see clearly that for both samples the first shell distance is far more similar to magnetite than hematite. This is significant because this shell denotes tetrahedral iron in magnetite, and octahedral iron in hematite. The first shell is located at 1.88 Å for the FeAG4.02 and FeAG3.07 samples, far closer to the 1.92 Å fitted for magnetite than the 1.98 Å for hematite (Table 4-4). Other sources report 1.89 Å for the first magnetite shell, which is even closer, and 1.93-1.94 Å for hematite which is even further away [55, 56]. The conclusion is that the first fitted oxygen shell denotes arises from tetrahedral iron.

The second shell varies between 2.06 Å for FeAG1, the same as magnetite, and 2.10 Å for FeAG7, closer to but still not near 2.18 Å for hematite, though other sources for hematite report 2.10 or even as close as 2.05 Å [55, 56]. In either case the second shell for, both model compounds, arise from octahedral iron sites. Overall, the samples seem closer to magnetite than hematite in regards to having a mixture of tetrahedral and octahedral sites. Assuming the second shell is octahedral we can calculate the fraction of tetrahedral sites. This is done by dividing the multiplicities of the first shells with four. The fractions becomes 0.43 for

FeAG4.02 and 0.65 for FeAG3.07, in both cases a higher fraction of 4-coordinated sites than the 0.33 for magnetite.

The conclusion from the XAS data is then that all samples contain predominantly Fe^{3+}. The K-edge position and pre-edge position together form a rather strong case, and we will go ahead and assume only Fe^{3+} as there is no evidence to the contrary. The coordination is strongly implied to be tetrahedral by XANES, but second oxygen shells are probably from octahedral sites. It is possible that the smaller contribution from octahedral sites to the pre-edge was hidden by the tetrahedral contribution. This is contradicted by the EXAFS results, as FeAG1 with a predicted 42% tetrahedral Fe^{3+} has a higher intensity pre-edge than FeAG7 at 65% when we would have expected the opposite [18]. One explanation could be that the second Fe-O shell denotes partially tetrahedral sites as well. This shell fits very well with our own and reported values for the second shell for magnetite [55], whose second shell is not tetrahedral iron, but it is important to remember that the species in question is clearly not magnetite. Magnetite is a black, ferromagnetic solid containing 1/3 Fe^{2+}, the samples are yellow-orange, exhibit no obvious magnetic properties and contain only Fe^{3+}. The nature of the iron species may be single sites, or it may be some nano-phase Fe_xO_y compound. It may also be a mixing of both.

5.3.1 Considering nano-phase

Of these possibilities, the most obvious is the presence of a nano-phase, as one is clearly visible in some of the XRD diffractograms. Especially the diffractogram for FeAG12 (figure 5-7) clearly show a diffraction pattern of five peaks. This pattern is fainter for the other gels, some peaks disappearing, but it still seems to be the same pattern in every case.

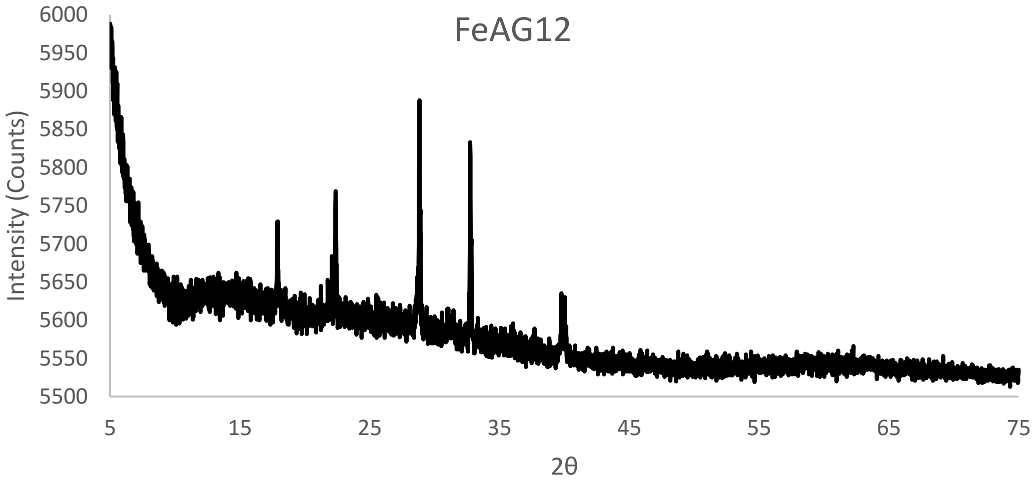

Figure 4-21: XRD diffractogram for sample FeAG12.

The pattern is strongest and most distinct for FeAG12, and seems to disappear with decreasing iron loading for samples from the same batch (see FeAG7-12 in figure 4-3). For FeAG3.07 the pattern is only evident by a very weak peak 29° 2θ. FeAG4.02 has a higher iron loading, but its diffractogram is featureless. Thus it is prudent to assume that even the apparently amorphous samples may contain very small particles of this crystalline nano-phase not detectable by XRD.

Unfortunately the origin of this diffractogram is unclear. The five peaks does not seem to obviously correspond to any other diffraction pattern found, though the peak at 33° 2θ is very close to a peak from hematite and the peak at 40° 2θ is the same for certain variants of ferrihydrite. Still, the similarities end there, and no other oxides or oxide-hydroxides seem to fit the remaining peaks. This includes maghemite, goethite, feroxyhyte and lepidococite. Ferrihydrite is perhaps the most logical suspect. It is a mixture of iron oxide and iron hydroxide known to appear from the precipitate of Fe(III) nitrate at neutral pH and be in an equilibrium with hematite [24]. Ferrihydrite has a poorly understood crystal structure and usually comes in two variants: 2-line and 6-line ferrihydrite. The names are derived from the XRD diffractograms which shows only two or six peaks respectively. Needless to say, neither is similar to the diffractogram for the FeAG samples.

The structure of ferrihydrite has been debated, and although several iron oxide-hydroxides like akageneite and goethite contain only octahedral Fe^{3+} it has been hypothesized that ferrihydrite contains tetrahedral iron due to the short first shell distance in EXAFS fitting of only 1.87-1.88 Å [23]. This shell distance is closer than for magnetite, and indeed exactly the value found for FeAG4.02, FeAG3.07 and maghemite, a partially tetrahedral iron(III) oxide [23]. This could help explain our tetrahedral iron species. The estimates of the tetrahedral site ratio in ferrihydrite is, however, only 20-30% [23]. This is far below the ones we have found for the samples, so it could not be the source of all the tetrahedral sites. To make the case for ferrihydrites worse, the second shell distance is slightly too long for the values reported for ferrihydrite or maghemite [23].

Iron hydroxides will form oxides during heat treating, so it is also possible that some ferrihydrite formed hematite or maghemite. Hematite is the more stable of the two and is known to form from ferrihydrite [24], but contains no tetrahedral sites. Maghemite does contain tetrahedral sites, but only 37.5%, barely enough to explain the expected 42% for FeAG4.02 and not enough for the 65% in FeAG3.07. This is assuming that all the iron species was maghemite, which would not agree with the EXAFS second shell distance [23], the XRD diffractogram or the magnetic properties of the samples, as maghemite is ferrimagnetic [23].

Ferrihydrite and maghemite contain tetrahedral sites, but neither can explain the prevalence of tetrahedral sites indicated by the EXAFS data. We must therefore find another way to explain the large ratio of tetrahedral site seen in the samples. Single sites may be a better explanation.

5.3.2 Considering single sites

Iron distributed into silica carriers is not abnormal, and has been introduced in both silica gels, zeolites, glasses and naturally occurring quartz as the gemstone citrine [19-22, 31]. With the exceptions of some mixed oxides [19] the general pattern is that interstitial Fe^{2+} prefers octahedral sites [22], while Fe^{3+} prefers tetrahedral sites [20-22].

As it is known that Fe^{3+} ions interact with SA to form complexes [27], and that Fe^{2+} will oxidise and then incorporate into silica gel when added to the sol-gel step [31], interstitial Fe^{3+} in the silica gel structure is a believable explanation for the extra tetrahedral sites.

EXAFS data for these single sites is sparse, except for Axon et Al. who analysed Fe^{3+} sites in ZSM-5 [21]. Axon et Al. reports only one fitted Fe-O shell at a short distance of 1.83 Å. This is shorter still than the 1.88 Å for our samples, and far shorter than magnetite. As ZSM-5 is not a pure silica structure it is uncertain how applicable this value is to silica aerogels, but the Si/Al ratio was roughly 20, so the material is mostly silica [21]. In any case, it at least implies that we should expect a short first shell distance, which is what we have seen so far.

To properly show the existence of single site iron in the samples we turn to the EXAFS results for the third and fourth shells. The fourier filtering shows that there is both a Fe···Fe shell and a Fe···Si shell. The Fe shell is closest at 3.06-3.07 Å for FeAG4.02 and FeAG3.07. The Si shell is farther away at 3.13-3.14 Å. This is very close to the reported 3.16 Å for the Fe···Si distance for incorporated Fe^{3+} in ZSM-5 [21]. If we assume that the Fe···Si shell represents single sites and the Fe···Fe shell represents nano-phase we can calculate the ratio of single sites like so:

$$r_{ss} = \frac{N_{Fe\cdots\mathrm{Si}}}{N_{Fe\cdots\mathrm{Si}} + N_{Fe\cdots\mathrm{Fe}}}$$

This leaves us with 60% single sites in FeAG4.02, and 64% single sites in FeAG3.07. The tetrahedral site ratio found by the first and second shell distances were 42% and 65% respectively. Assuming that all single sites are tetrahedral, and thus contribute to the first shell

[21], we can now explain the origin of all the predicted tetrahedral sites. The main issue is FeAG1 where our prediction is too high. We will address this issue later.

So far we have discussed interstitial Fe^{3+}, but Lopez et Al. discusses Fe^{3+} interacting with the silica surface [31]. They propose that Fe^{3+} ions interact with silanol groups. The proposed result is solitary Fe^{3+} forming octahedral complexes partially bonded to bidentate silica ligands. The scenario is somewhat doubtful for APD aerogels as the surface of the gels would be hydrophobic, and most silanol groups would be inaccessible for forming ligands. Even if complexes formed during the sol-gel step they would be relatively loosely bound compared to the competing covalent bonds from HMDSO and HMDZ and they may have been largely removed during surface modification. On the other hand, the presence of surface bound iron complexes could be blocking the surface modification, which could explain the increasing shrinkage seen at higher iron loadings.

If these octahedral sites were present, they could increase the apparent single site ratio while decreasing the tetrahedral site ratio. This could help explain the large number of predicted single sites for FeAG4.02 at 60%, but the low ratio of tetrahedral sites at 42%. This does not explain why this is not seen in FeAG3.07 as well. The samples have similar iron loadings, and FeAG4.02 had more silylation reagents added during synthesis, which logically should decrease such surface interaction, and certainly not improve it. There is another, far more likely explanation, if we consider both single sites and bulk phase.

5.3.3 Considering a nano-phase and single sites combination

The XRD data shows the presence of a crystalline bulk phase. The EXAFS data show a high ratio of single sites, as well as bulk phase. The UV-vis results show a CT feature at 200-300 nm for all samples implying solitary Fe^{3+} [29-31] as well as a tail feature at higher wavelength implying bulk phase [32, 46], and the overall colour is very similar to citrine known to contain single sites and Fe_xO_y clusters [22]. The implication is very strong that both are present in the samples, and considering them in combination resolves issues neither scenario could on their own.

The samples have roughly 60-65% predicted single sites, which would naturally also mean 35-40% predicted nano-phase. There is a problem predicting this ratio, however, and that problem arises when the bulk phase is in the form of very small particles. As particles grow smaller the iron atoms close to the surface would represent a larger fraction than those in the centre. These surface atoms are not fully coordinated beyond the oxygen shells. This means that the single site ratio is too high depending on the size of the bulk particles.

FeAG4.02 has no evident crystallinity in the XRD diffractograms, but the EXAFS still imply some Fe···Fe interactions. This would imply that the bulk particles are very small, leading to the single site fraction being overestimated. The same effect is probably present in FeAG7, but to a smaller degree, as the XRD diffractogram for FeAG7 shows a hint a crystallinity implying larger particles.

This is the most likely scenario we have discussed. Tetrahedral single sites account for most of the first Fe-O shell, and small particles of iron oxide/hydroxide largely represents the octahedral sites as well as decreasing the actual Fe···Fe multiplicity due to their small size [26]. We do not know the exact constituents of these particles, but it is most likely a mixture of a form of iron oxide-hydroxide, possibly similar to ferrihydrite, and the iron oxide hematite [24]. The first Fe-O shell distance is not as low as expected [21], and it may be a compromise with the higher Fe-O distances of these other bulk compounds [23, 24, 55].

Additionally not all tetrahedrally coordinated iron has to be single sites, as some could result from the Fe_xO_y nano-phase [23]. Similarly not all single sites must be tetrahedral, they could also be octahedral in the form of silanol complexes [31]. We have no evidence to determine if either of these cases are true, or to what degree they would contribute.

6 Conclusion

Incorporating Fe^{3+} into silica aerogels synthesized from waterglass, surface modified and dried by the APD method produces samples of descent porosity with single site Fe^{3+} incorporated in the silica and some small nano-clusters of an unknown Fe_xO_y species, most likely similar to ferrihydrite. The single sites are likely tetrahedral in coordination, though some octahedral single sites may also occur on the silica surface. The nano-sized clusters of Fe_xO_y are most likely octahedral.

Annealing the samples removes the hydrophobic surface modification allowing for increased interaction between Fe_xO_y and the silica surface. This is accompanied by a sharp decrease in Fe_xO_y particle size, though the exact mechanism behind it is unknown.

Adding Fe^{3+} to silica aerogels increases the average pore diameter compared to plain silica aerogels and a increase in porosity. Increasing the iron loading further will cause the porosity to eventually drop below that of plain gels. Increased iron content also increases the apparent size and crystallinity of the Fe_xO_y particles though whether it also increases the single site population is uncertain.

7 Future Work

A proper parameter study could be helpful to understand the synthesis reactions and mechanisms as well as allowing us more control over the end products. SA is a difficult parameter to control, but gauging the concentration by pH could work. pH could also be its own parameter, controlled by adding ammonia or nitric acid as ammonium and nitrate are already present anyway. We would also recommend synthesises with lower iron content than what is used here to see if a gel with only single sites can be made.

The precipitation of Fe_xO_y species is most likely due to irons tendency to form hydroxides at higher pH. Performing an acid catalysed synthesis could potentially circumvent this problem and would be worth a try. Acid catalysis would unfortunately force us to use the derivatization method and give up the advantages of the co-precursor method.

Additional characterization would be helpful, especially characterising the surface before and after annealing, as this is where a lot of interesting changes take place. IR spectroscopy, TGA and electron microscopy could be helpful techniques. Getting good EXAFS data for annealed gels as well as a larger range of gels with different iron content would also be very interesting.

Catalytic testing should be done on this material, especially OCM and SCR reactions.

8 Sources

1. Warren, S.C., et al., *A silica sol–gel design strategy for nanostructured metallic materials.* Nat Mater, 2012. **11**(5): p. 460-467.
2. Zheng, X., et al., *Ultralight, ultrastiff mechanical metamaterials.* Science, 2014. **344**(6190): p. 1373-1377.
3. Gurav, J.L., et al., *Silica aerogel: synthesis and applications.* J. Nanomaterials, 2010. **2010**: p. 1-11.
4. Bhagat, S.D., et al., *Rapid synthesis of water-glass based aerogels by in situ surface modification of the hydrogels.* Applied Surface Science, 2007. **253**(6): p. 3231-3236.
5. Kristiansen, T., et al., *Single-Site Copper by Incorporation in Ambient Pressure Dried Silica Aerogel and Xerogel Systems: An X-ray Absorption Spectroscopy Study.* The Journal of Physical Chemistry C, 2011. **115**(39): p. 19260-19268.
6. Kristiansen, T. and K. Mathisen, *On the Promoting Effect of Water during NO x Removal over Single-Site Copper in Hydrophobic Silica APD-Aerogels.* The Journal of Physical Chemistry C, 2014. **118**(5): p. 2439-2453.
7. Kristiansen, T., et al., *There and Back Again: The Unique Nature of Copper in Ambient Pressure Dried-Silica Aerogels.* The Journal of Physical Chemistry C, 2012. **116**(38): p. 20368-20379.
8. Heurtefeu, B., et al., *Single-Site Catalysts*, in *Encyclopedia of Polymer Science and Technology*. 2002, John Wiley & Sons, Inc.
9. Zecchina, A.B., S.; Groppo, E., *Selective Nanocatalysts and Nanoscience: Concepts for Heterogeneous and Homogeneous Catalysis*. 2011: Wiley.
10. Guo, X., et al., *Direct, Nonoxidative Conversion of Methane to Ethylene, Aromatics, and Hydrogen.* Science, 2014. **344**(6184): p. 616-619.
11. Ruitenbeek, M. and B.M. Weckhuysen, *A Radical Twist to the Versatile Behavior of Iron in Selective Methane Activation.* Angewandte Chemie International Edition, 2014. **53**(42): p. 11137-11139.
12. Kistler, S., *Coherent expanded-aerogels.* The Journal of Physical Chemistry, 1932. **36**(1): p. 52-64.
13. Schaefer, D.W. and K.D. Keefer, *Structure of random porous materials: silica aerogel.* Physical review letters, 1986. **56**(20): p. 2199.

14. Soleimani Dorcheh, A. and M.H. Abbasi, *Silica aerogel; synthesis, properties and characterization.* Journal of Materials Processing Technology, 2008. **199**(1–3): p. 10-26.

15. Chorkendorff, I.N., J.W., *Concepts of Modern Catalysis and Kinetics*. 2nd ed. 2007: Wiley-VCH.

16. Maleki, H., L. Durães, and A. Portugal, *An overview on silica aerogels synthesis and different mechanical reinforcing strategies.* Journal of Non-Crystalline Solids, 2014. **385**: p. 55-74.

17. Rao, A.V. and R.R. Kalesh, *Organic Surface Modification of TEOS Based Silica Aerogels Synthesized by Co-Precursor and Derivatization Methods.* Journal of Sol-Gel Science and Technology. **30**(3): p. 141-147.

18. Wilke, M., et al., *Oxidation state and coordination of Fe in minerals: An Fe K-XANES spectroscopic study.* American Mineralogist, 2001. **86**(5-6): p. 714-730.

19. Calas, G. and J. Petiau, *Coordination of iron in oxide glasses through high-resolution K-edge spectra: information from the pre-edge.* Solid state communications, 1983. **48**(7): p. 625-629.

20. Inui, T., et al., *Environments of Iron in Fe-Silicates Synthesized by the Rapid Crystallization Method.* Journal of Catalysis, 1993. **139**(2): p. 482-489.

21. Axon, S.A., et al., *EXAFS studies of iron-substituted zeolite ZSM-5.* Chemical Physics Letters, 1992. **189**(1): p. 1-6.

22. Lehmann, G., *Yellow color centers in natural and synthetic quartz.* Physik der kondensierten Materie, 1971. **13**(4): p. 297-306.

23. Maillot, F., et al., *New insight into the structure of nanocrystalline ferrihydrite: EXAFS evidence for tetrahedrally coordinated iron(III).* Geochimica et Cosmochimica Acta, 2011. **75**(10): p. 2708-2720.

24. Manceau, A. and V. Drits, *Local structure of ferrihydrite and feroxyhite by EXAFS spectroscopy.* Clay minerals, 1993. **28**: p. 165-165.

25. Pokrovski, G.S., et al., *Iron (III)-silica interactions in aqueous solution: insights from X-ray absorption fine structure spectroscopy.* Geochimica et Cosmochimica Acta, 2003. **67**(19): p. 3559-3573.

26. Kuśtrowski, P., et al., *Catalytic Activity of MCM-48-, SBA-15-, MCF-, and MSU-Type Mesoporous Silicas Modified with Fe3+ Species in the Oxidative Dehydrogenation of Ethylbenzene in the Presence of N2O.* The Journal of Physical Chemistry A, 2005. **109**(43): p. 9808-9815.

27. Porter, R.A. and W.J. Weber, *The interaction of silicic acid with iron(III) and uranyl ions in dilute aqueous solution.* Journal of Inorganic and Nuclear Chemistry, 1971. **33**(8): p. 2443-2449.
28. Schindler, P., et al., *Ligand properties of surface silanol groups. I. Surface complex formation with Fe 3+, Cu 2+, Cd 2+, and Pb 2+.* Journal of Colloid and Interface Science, 1976. **55**(2): p. 469-475.
29. Jitianu, A., et al., *Influence of the silica based matrix on the formation of iron oxide nanoparticles in the Fe 2 O 3–SiO 2 system, obtained by sol–gel method.* Journal of Materials Chemistry, 2002. **12**(5): p. 1401-1407.
30. Fabrizioli, P., et al., *Synthesis, structural and chemical properties of iron oxide–silica aerogels.* Journal of Materials Chemistry, 2002. **12**(3): p. 619-630.
31. López, T., et al., *Spectroscopic study of sol-gel silica doped with iron ions.* Materials Chemistry and Physics, 1992. **30**(3): p. 161-167.
32. Bongiovanni, R., et al., *On the formation of iron(III) oxides via oxidation of iron(II),* in *Other Information: PBD: [1994]*. 1994. p. Medium: ED; Size: 25 p.
33. Dunn, B.C., et al., *Silica aerogel supported catalysts for Fischer–Tropsch synthesis.* Applied Catalysis A: General, 2005. **278**(2): p. 233-238.
34. Owens, L., T.M. Tillotson, and L.M. Hair, *Characterization of vanadium/silica and copper/silica aerogel catalysts.* Journal of Non-Crystalline Solids, 1995. **186**: p. 177-183.
35. Casula, M.F., A. Corrias, and G. Paschina, *Iron oxide–silica aerogel and xerogel nanocomposite materials.* Journal of Non-Crystalline Solids, 2001. **293–295**: p. 25-31.
36. Popovici, M., et al., *Ultraporous Single Phase Iron Oxide−Silica Nanostructured Aerogels from Ferrous Precursors.* Langmuir, 2004. **20**(4): p. 1425-1429.
37. Fabrizioli, P., T. Bürgi, and A. Baiker, *Environmental Catalysis on Iron Oxide–Silica Aerogels: Selective Oxidation of NH3 and Reduction of NO by NH3.* Journal of Catalysis, 2002. **206**(1): p. 143-154.
38. Bauer, J., *A Field Guide to Minerals, Rocks and Precious Stones*. 1987: Treasure Press.
39. Sing, K.S., *Reporting physisorption data for gas/solid systems with special reference to the determination of surface area and porosity (Recommendations 1984).* Pure and applied chemistry, 1985. **57**(4): p. 603-619.

40. Rouquerol, J., et al., *Recommendations for the characterization of porous solids (Technical Report).* Pure and Applied Chemistry, 1994. **66**(8): p. 1739-1758.

41. Brunauer, S., P.H. Emmett, and E. Teller, *Adsorption of gases in multimolecular layers.* Journal of the American chemical society, 1938. **60**(2): p. 309-319.

42. Barrett, E.P., L.G. Joyner, and P.P. Halenda, *The Determination of Pore Volume and Area Distributions in Porous Substances. I. Computations from Nitrogen Isotherms.* Journal of the American Chemical Society, 1951. **73**(1): p. 373-380.

43. Taylor, H.E., *Inductively Coupled Plasma-Mass Spectrometry*. 2001: Academic Press.

44. Peter Atkins, T.O., Jonathan Rourke, Mark Weller, Fraser Armstrong, *d-metal Complexes: Electronic Structure and Properties*, in *Shriver & Atkins' Inorganic Chemistry*. 2010, Oxford University Press. p. 473-506.

45. Tippins, H., *Charge-transfer spectra of transition-metal ions in corundum.* Physical Review B, 1970. **1**(1): p. 126.

46. Bordiga, S., et al., *XANES study of Ti and Fe substituted silicalites in presence and in absence of NH3 and comparison with UV-vis, IR and Raman spectra.* Nuclear Instruments and Methods in Physics Research Section B: Beam Interactions with Materials and Atoms, 1995. **97**(1–4): p. 23-27.

47. Bordiga, S., et al., *Structure and Reactivity of Framework and Extraframework Iron in Fe-Silicalite as Investigated by Spectroscopic and Physicochemical Methods.* Journal of Catalysis, 1996. **158**(2): p. 486-501.

48. Newville, M., *Fundamentals of XAFS. Consortium for Advanced Radiation Sources.* University of Chicago, Chicago, IL, 2004.

49. Mottana, A. and A. Marcelli, *The historical development of X-ray Absorption Fine Spectroscopy and of its applications to Materials Science*, in *A Bridge between Conceptual Frameworks*. 2015, Springer. p. 275-301.

50. Rupp, B.W., J., *X-ray K- and L-edge Energies of the Elements, eV.* Exafs Materials.

51. Waychunas, G.A., M.J. Apted, and G.E. Brown Jr, *X-ray K-edge absorption spectra of Fe minerals and model compounds: near-edge structure.* Physics and Chemistry of Minerals, 1983. **10**(1): p. 1-9.

52. Galoisy, L., G. Calas, and M. Arrio, *High-resolution XANES spectra of iron in minerals and glasses: structural information from the pre-edge region.* Chemical geology, 2001. **174**(1): p. 307-319.

53. Lee, P., et al., *Extended x-ray absorption fine structure—its strengths and limitations as a structural tool.* Reviews of Modern Physics, 1981. **53**(4): p. 769.

54. Teo, B. and D. Joy, *EXAFS spectroscopy.* Techniques and Applications, 1981.

55. Corrias, A., et al., *An X-ray absorption spectroscopy study of the Fe K edge in nanosized maghemite and in Fe 2 O 3–SiO 2 nanocomposites.* Physical Chemistry Chemical Physics, 2000. **2**(5): p. 1045-1050.

56. Wong, S.-T., et al., *In-situ study of MCM-41-supported iron oxide catalysts by XANES and EXAFS.* Applied Catalysis A: General, 2000. **198**(1–2): p. 115-126.